MULTIFIDELITY, MULTIDISCIPLINARY OPTIMIZATION OF TURBOMACHINES WITH SHOCK INTERACTION

A Dissertation

by

MICHAEL MARIE JOLY

Submitted to the Office of Graduate and Professional Studies of
Texas A&M University
in partial fulfillment of the requirements for the degree of

DOCTOR OF PHILOSOPHY

Chair of Committee,	Paul Cizmas
Committee Members,	John Keyser
	Guillermo Paniagua
	Othon Rediniotis
	William Saric
	Tom Verstraete
Head of Department,	Rodney Bowersox

August 2014

Major Subject: Aerospace Engineering

ABSTRACT

Research on high-speed air-breathing propulsion aims at developing aircraft with antipodal range and space access. Before reaching high speed at high altitude, the flight vehicle needs to accelerate from takeoff to scramjet takeover. Air turbo rocket engines combine turbojet and rocket engine cycles to provide the necessary thrust in the so-called low-speed regime. Challenges related to turbomachinery components are multidisciplinary, since both the high compression ratio compressor and the powering high-pressure turbine operate in the transonic regime in compact environments with strong shock interactions. Besides, lightweight is vital to avoid hindering the scramjet operation.

Recent progress in evolutionary computing provides aerospace engineers with robust and efficient optimization algorithms to address concurrent objectives. The present work investigates Multidisciplinary Design Optimization (MDO) of innovative transonic turbomachinery components. Inter-stage aerodynamic shock interaction in turbomachines are known to generate high-cycle fatigue on the rotor blades compromising their structural integrity. A soft-computing strategy is proposed to mitigate the vane downstream distortion, and shown to successfully attenuate the unsteady forcing on the rotor of a high-pressure turbine. Counter-rotation offers promising prospects to reduce the weight of the machine, with fewer stages and increased load per row. An integrated approach based on increasing level of fidelity and aero-structural coupling is then presented and allows achieving a highly loaded compact counter-rotating compressor.

ACKNOWLEDGMENTS

The work presented herein, as well as the valuable insight gained that led me to this point, arose from the generosity of several people.

I begin by thanking my advisor, Dr. Paul Cizmas, which made my graduate studies at Texas A&M University possible. He provided me guidance and support with my research, and in addition to sharing his time and insight, continuously challenged me.

This work is the result of collaborative efforts made between Texas A&M Univeristy and the von Karman Institute for Fluid Dynamics. I would like to thank Dr. Guillermo Paniagua and Dr. Tom Verstraete, my advisors at the von Karman Institute, for their continuous assistance, feedbacks and support.

I additionally thank the members of my committee for their time and valuable feedbacks. Drs John Keyser, Othon Rediniotis, and William Saric's knowledge and interest in my work has been much appreciated.

Discussions with Dr. Girimaji of Texas A&M University and Dr. Barassa of AVL List GmbH contributed to help me gaining extended understanding about turbulence modeling, and I sincerely appreciated their assistance and feedbacks.

This work has been funded initially through the LAPCAT II European research project. I would like to thank Dr. Johan Steelant of the European Space Agency for his feedbacks during project meetings. The Gustave Boel - Sofina Fellowship of the Belgian American Educational Foundation has then been an important support to initiate joint studies between the von Karman Institute and Texas A&M University. I really appreciated the follow-up of Marie-Claude Hayoit and Dr. Emile Boulpaep. The Aerospace Propulsion and Energy Systems Fellowship of Texas A&M University

was eventually an essential support to bring this work to completion.

My fellow graduate students throughout the years have also played an important role in my graduate studies. I would like to thank my colleagues from the von Karman Institute, Boris, Erik, Alessandro, Domingo, Lasse, Christopher, Sebastian, and from Texas A&M University, Raymond, Brian, Robert, Neil, Forrest, and David.

Finally, I would like to thank my family and friends for their unconditional and unending support. I am especially thankful to my parents for their many sacrifices and for teaching me the benefits of hard work. I also thank my wife, who has always been patient and supporting during my studies. They are all the reason for my success.

TABLE OF CONTENTS

Page

LIST OF FIGURES

FIGURE Page

FIGURE Page

LIST OF TABLES

1. INTRODUCTION*

1.1 Turbomachinery for high-speed propulsion

1.1.1 Air turbo rocket from take-off to scramjet operation

Research on hypersonic air-breathing propulsion aims at developing aircrafts with antipodal range and space access [1]. Air Turbo Rocket (ATR) engines provide the necessary thrust in the so-called low speed regime (from takeoff to scramjet takeover). This technology uses a fan similar to those found in high bypass turbojet engines with the particularity that high compression ratios are required to limit the size of the engine [2]. The fan is powered by a high-pressure turbine, which expands the preheated fuel. In both components, higher load per blade row allows to reduce the number of stages. However, an increase of load implies that the flow across the blade passages is transonic, resulting in shock interactions.

1.1.2 Concurrent multidisciplinary challenges

Flows around turbines and compressors are three-dimensional, compressible and turbulent. Various fluid dynamics phenomena occur within a blade row and interact with each other, including boundary layer growth and transition, secondary flows, wakes, expansion fans, and shock waves. Inter-row shock interactions become critical in high-pressure turbomachinery components. Strong shock waves impingements on

*Reprinted with permission from "Differential evolution based soft optimization to attenuate vane-rotor shock interaction in high-pressure turbines" by Joly, M. M. Verstraete T. and Paniagua G., *Applied Soft Computing*, Vol. 13, No. 4, 2013, pp. 1882–1891, Copyright 2013 by Elsevier, from "Multidisciplinary design optimization of a compact highly loaded fan" by Joly, M. M. Verstraete T. and Paniagua G., *Structural and Multidisciplinary Optimization*, Vol. 49, No. 3, 2013, pp. 471–483, DOI: 10.1007/s00158-013-0987-5, Copyright 2013 by Springer, and from "Integrated multifidelity, multidisciplinary evolutionary design optimization of counterrotating compressors" by Joly, M. M. Verstraete T. and Paniagua G., *Integrated Computer-Aided Engineering*, Vol. 21, 2014, pp. 249–261, DOI: 10.3233/ICA-140463, Copyright 2014 by IOS Press.

the surface of rotors cause pressure and temperature fluctuations, subsequently leading to high-cycle fatigue and potential catastrophic failure of the blades. The design, optimization and control of high-pressure turbomachinery require multi-disciplinary approaches, where both aerodynamics performance and structural integrity are considered.

1.2 Multi-disciplinary analysis and optimization

A review of methods for Computational Fluid Dynamics (CFD) and Multidisciplinary Design Optimization (MDO) suitable for turbomachinery applications is proposed in this section.

1.2.1 Computational fluid dynamics

Turbomachinery high-speed stages operate at high Reynolds number, where boundary layer transition is usually triggered early on the blade profile. The complex nature of turbulent flows makes the approximations of boundary layers by mathematical models a challenging task. An ideal turbulence model should introduce the minimum amount of complexity while capturing the essence of the relevant physics [3].

The prediction of turbulent flows improves as one attempts to resolve the large and small scales of turbulence, in contrast from model prediction. By increasing levels of fidelity and complexity, the following main methods can be considered: Unsteady Reynolds-Averaged Navier-Stokes (URANS), Detached Eddy Simulation (DES), Variable-Resolution (VR), Large Eddy Simulation (LES), and Direct Numerical Simulation (DNS). Between the limit of URANS that still relies on turbulence modeling, and the computational burden of the eddy-resolving LES and DNS solvers, hybrid methods are becoming increasingly attractive. However, despite the continually increasing computational power, the numerical resolution of turbulence remains

computationally intractable with modern computers. Steady turbulent modeling remains therefore the most viable approach for aerodynamic optimization. Recent models for Reynolds-Averaged Navier-Stokes (RANS) have been proposed and provide interesting prospects for turbomachinery applications.

1.2.2 Multidisciplinary design optimization

Innovative optimization and design techniques for engine systems aim maximum performance in a multidisciplinary context. Especially, turbomachinery exhibits a multitude of multi-physics problems. Coupled with CFD solvers, Computational Structure Mechanics (CMS) and Conjugate Heat Transfer (CHT) analysis allow to predict the behavior of blades subject to aero-structural and aero-thermal excitations, respectively. Similarly to eddy resolving turbulent solver, coupled analysis remain extremely expensive and their integration into optimization challenging.

Notable progress has been made over the last decades on Multidisciplinary Design Optimization (MDO) techniques. Evolutionary Algorithms (EAs) are particularly suitable for the design optimization of novel complex turbomachinery components. Conventional optimization techniques, such as gradient-based methods, are difficult to extend to multi-objective cases; in practice, multi-objective problems have to be reformulated as single-objective prior to optimization [4]. They are also subject to the risk of being trapped in a local minimum, where the solution could only be in the neighborhood of the starting point [5]. Alternatively, EAs can handle complex problems, involving features such as discontinuities, multi-modality, disjoint feasible spaces and noisy function evaluations. Based on Darwinian evolution, populations of individuals evolve and adapt to the environment through the use of mutation, crossover, and selection. The individuals with a higher fitness are more likely to survive and/or reproduce.

Research to enhance diversity, robustness, convergence, as well as the handling of high-dimensional problems with multiple objectives and constraints is ongoing. Early contributions addressed, but not exclusively, constraint handling [6], surrogate model assistance [7], and parallelism [8]. More recent trends include evolutionary optimization under uncertainties [9] and knowledge-based evolution guidance [10]. Evolutionary computing is an active field research and has a continuous substantial impact on the computational engineering of complex systems.

1.3 Approach and novel contributions

The scope of this dissertation is to investigate methodologies for aero-structural optimization of transonic turbines and compressors, with three main objectives:

- Evaluation of ν, k-ω, k-ϵ, and k-ϵ-v^2-f turbulence models
- Attenuation of unsteady shock interaction in high-pressure turbines
- Multi-fidelity, multi-disciplinary design optimization of counter-rotating fans

1.3.1 Modeling wall-bounded turbulent flows

Advancements in CFD solvers consist of techniques for grid generation, discretization schemes and algorithms, and turbulence modeling and/or resolution. A first part of this dissertation focuses on the evaluation of turbulence models for turbomachinery optimization. Popular turbulence models in the turbomachinery community are the one-equation model of Spalart-Allmaras [11] and the two-equation SST k-ω model of Menter [12]. The first part of this dissertation evaluates these models, as well as the more recent k-ϵ-v^2-f turbulence model, and their potential benefits for turbomachinery performance evaluations.

1.3.2 Soft optimization of unsteady turbine shock interaction

High-pressure turbines experience strong vane-rotor interactions. Several attempts to mitigate the unsteady shock interaction are detailed in the literature, including investigations for enhanced physical understanding, active control systems, and numerical optimizations with neural networks. The unsteady optimization of real three-dimensional geometries remains however unpractical with modern computers, even with the assistance of surrogate models. In a second part of this dissertation, a soft-computing optimization method is presented to attenuate the unsteady forcing on the rotors using evolutionary optimization. It is proposed to modulate the pitch-wise static pressure distribution downstream of the stand-alone vane, and alter the vane contraction channel to mitigate the downstream propagation of shock waves. The approach is validated with the assessment of unsteady forcing abatement on the downstream rotor.

1.3.3 Multi-disciplinary design optimization for counter-rotation

Counter-rotation offers the perspective to reduce the size and weight of aircraft engines, by introducing two opposite spinning directions and suppressing stator rows in-between two consecutive rotors. Research on counter-rotation in turbomachinery is emerging and faces multidisciplinary challenges. In stator-less machines, the subsequent higher load on rotors strengthens the need of aero-structural evaluations. The third part of this dissertation proposes a MDO strategy for counter-rotating compressors. The key is to use the benefits of evolutionary computing to smooth the handover between the preliminary design and the three-dimensional geometry definition with a novel parameterization based on span-wise distributions. It provides flexible ranges for the design of the detailed geometry within the optimization process, which alleviates the presence of infeasible regions due to the unique inci-

dence in supersonic passages. The method also comprises increasing level of fidelity and coupled static aero-structural evaluations. Eventually, this approach allows the concurrent design of the two rotors.

1.4 Accomplishments

• Developed a Navier-Stokes multi-block solver with ν, k-ω, k-ϵ, and k-ϵ-v^2-f turbulence models

• Proposed a soft computing approach to mitigate unsteady shock interaction in high-pressure turbines

• Proposed a MDO approach for the design and optimization of counter-rotating compressors, based on a span-wise geometry parameterization, a multi-fidelity design optimization strategy, and static aero-structural evaluations

2. TURBULENCE MODELS FOR TURBOMACHINERY

This chapter presents the development of a Reynolds-Averaged Navier-Stokes (RANS) solver, in which different turbulent models are implemented. Comparison between the models is performed with the turbulent flows on a flat plate and around a high-pressure turbine vane.

2.1 Introduction

2.1.1 Turbulence models in RANS equations

The steady state of compressible turbulent flows can be simulated by the Favre- and Reynolds-Averaged Navier-Stokes equation (equation 2.1).

$$\begin{aligned}
&\frac{\partial \overline{\rho}}{\partial t} + \frac{\partial}{\partial x_i}(\overline{\rho}\,\tilde{v}_i) = 0 \\
&\frac{\partial}{\partial t}(\overline{\rho}\,\tilde{v}_i) + \frac{\partial}{\partial x_j}(\overline{\rho}\,\tilde{v}_j\tilde{v}_i) = -\frac{\partial \overline{p}}{\partial x_i} + \frac{\partial}{\partial x_j}\left(\bar{\tau}_{ij} - \overline{\rho}\,\widetilde{v_i'' v_j''}\right) \\
&\frac{\partial}{\partial t}(\overline{\rho}\tilde{E}) + \frac{\partial}{\partial x_j}(\overline{\rho}\,\tilde{v}_j\tilde{H}) = \frac{\partial}{\partial x_j}\left(k\frac{\partial \tilde{T}}{\partial x_j} - \overline{\rho}\,\widetilde{v_j'' h''} + \widetilde{\tau_{ij} v_i''} - \overline{\rho}\,\widetilde{v_j'' K}\right) \\
&\qquad\qquad + \frac{\partial}{\partial x_j}\left[\tilde{v}_i\left(\bar{\tau}_{ij} - \overline{\rho}\,\widetilde{v_i'' v_j''}\right)\right] .
\end{aligned} \tag{2.1}$$

These equations exhibit a turbulence closure problem, where the non-linear term $\widetilde{v_i'' v_i''}$ needs to be modeled. The eddy-viscosity hypothesis of Boussinesq assumes the turbulent shear stress to relate linearly to mean rate of strain, as expressed in equation 2.2, with S_{ij} the strain-rate tensor, K the turbulent kinetic energy, and μ_T the eddy viscosity. The latter requires additional equations to be determined, and

several turbulence models have been proposed.

$$\tau_{ij}^{F} = -\overline{\rho}\,\widetilde{v_i'' v_j''} = 2\mu_T \tilde{S}_{ij} - \left(\frac{2\mu_T}{3}\right)\frac{\partial \tilde{v}_k}{\partial x_k}\delta_{ij} - \frac{2}{3}\overline{\rho}\tilde{K}\delta_{ij} \tag{2.2}$$

2.2 Implementation of ν, k-ω, k-ϵ, and k-ϵ-v^2-f models

A preliminary step toward the implementation of different turbulent models is the development of a laminar, viscous solver. Subsequently, different turbulence models are considered: Spalart-Allmaras, SST k-ω, Chien k-ϵ, and k-ϵ-v^2-f.

2.2.1 Laminar, viscous flow solver

A two-dimensional multi-block finite volume viscous solver for laminar flows is developed. The structure of the code employs the object-oriented capacities of the language C++, allowing the convenient generation of multiple instances of blocks, cells and faces. The Roe's flux-difference splitting scheme is implemented for the spatial discretization of convective fluxes. The derivatives of viscous fluxes are approximated using the Green's theorem. A four-stage Runge Kutta scheme is used for the explicit time integration. Acceleration techniques, such local time stepping, multi-grid, and implicit residual smoothing, are implemented.

2.2.2 Turbulent flow solver

The solver is complemented with turbulence models. The model of Spalart-Allmaras [11] is first implemented. It employs one transport equation for an eddy-viscosity variable $\tilde{\nu}$ [13]. The two-equation SST k-ω model of Menter [12] and the k-ϵ model with the Chien's damping functions [14] complement the suite of popular models for turbomachinery.

A four-equation model was proposed by Durbin [15] and enhances two-equation

models for the purpose of improved near-wall behavior, with an additional equation for the velocity scale v^2 and an equation for the elliptic relaxation function f. The version implemented (model 3 in [16]) includes modifications from the original version, decoupling the ϵ and f wall boundary conditions, leading to equation 2.3. The v^2 equation is treated the same way as other transport equations. The elliptic relaxation function f is a modified Helmhotz-type equation, whose linear system is solved with a 5-diagonal matrix after discretization of the laplacian operator on each cell using the Gauss's theorem.

$$\begin{aligned}
\partial_t k &= \frac{1}{\rho}\nabla\cdot[(\mu+\mu_t)\nabla k] - U\cdot\nabla k + P_k - \epsilon \\
\partial_t \epsilon &= \frac{1}{\rho}\nabla\cdot\left[(\mu+\frac{\mu_t}{\sigma_\epsilon})\nabla\epsilon\right] - U\cdot\nabla\epsilon + \frac{C^*_{\epsilon 1}P_k - C_{\epsilon 2}\epsilon}{T} \\
\partial_t \overline{v^2} + U\cdot\nabla\overline{v^2} &= \frac{1}{\rho}\nabla\cdot\left[(\mu+\frac{\mu_t}{\sigma_k})\nabla\overline{v^2}\right] + k\tilde{f} - 6\frac{\epsilon}{k}\overline{v^2} \\
\tilde{f} - L^2\nabla^2\tilde{f} &= \frac{C_1}{T}\left[\frac{2}{3} - \frac{\overline{v^2}}{k}\right] + C_2\frac{P_k}{k} + 5\frac{\overline{v^2}}{kT}
\end{aligned} \tag{2.3}$$

2.3 Results

The different turbulence models are compared with the flows on a flat plate and around a high-pressure turbine vane.

2.3.1 Turbulent flow over a flat plate

This test case is based on experimental data from Wieghardt [17] at a Mach number of 0.09697 and a Reynolds number of Re=1.8x10^6. The grid employed is illustrated in Figure 2.1, which also details the boundary conditions applied. The four turbulence models exhibit very comparable predictions of velocity profiles on a flat plate (see Figure 2.2). The profiles compares well with experimental data, as

well as theoretical profiles (viscous sub-layer and law of the wall).

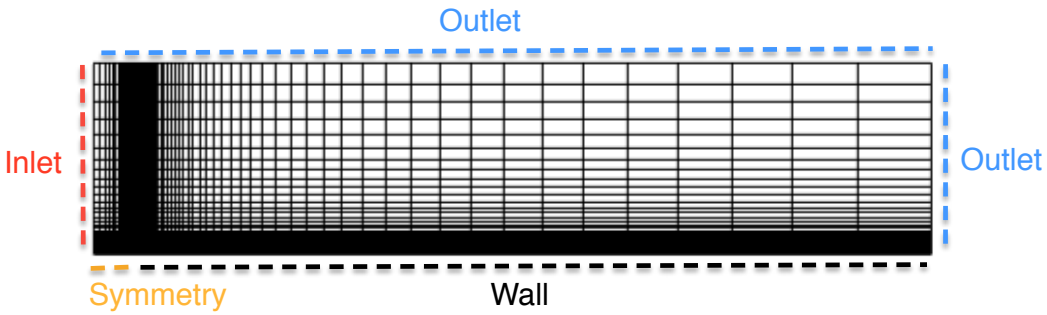

Figure 2.1: Grid and boundary conditions for flat plate flow

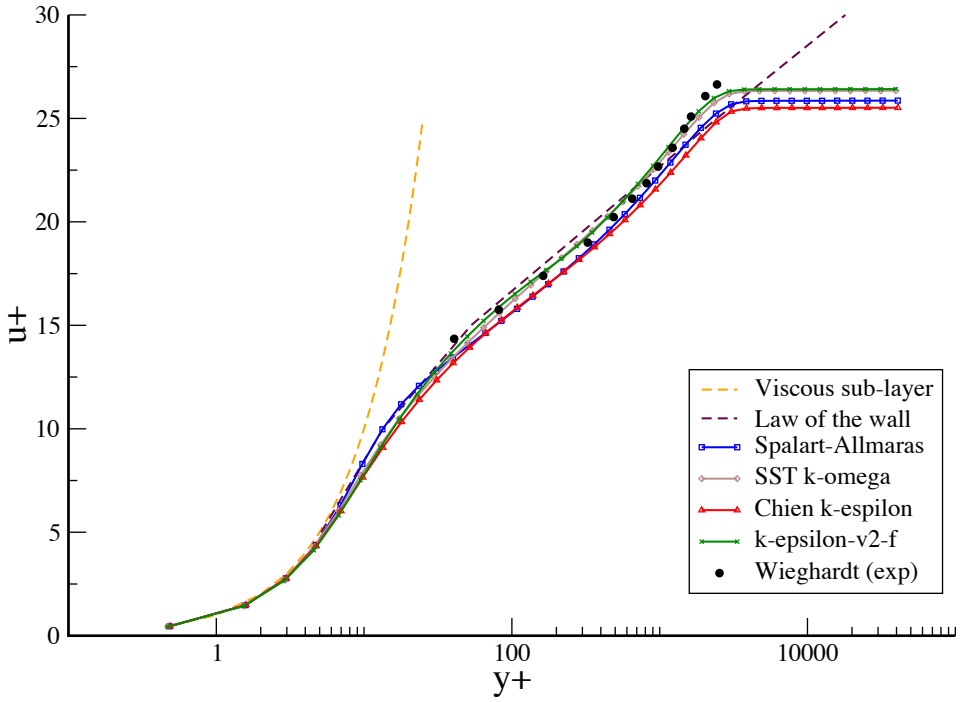

Figure 2.2: Turbulent flow over a flat plate

2.3.2 Turbulent flow around a high-pressure turbine vane

The second test case is the CT3 turbine vane of the von Karman Institute. Inlet boundary conditions are P0=162000Pa, T0=440K, and zero flow angle. The pressure at the outlet is determined from an isentropic Mach number of 1.2. A five-block topology is developed and shown on Figure 2.3, which also highlights the periodic boundary condition. Figures 2.4 and 2.5 illustrate the grid refinement around the blade, in the wake area, and in the throat area. The predicted Mach number field is shown on Figure 2.6. Good agreement with experiment isentropic Mach number distributions around the blade is obtained with the Spalart-Allmaras and Chien k-ϵ turbulence models (See Figure 2.7). The Spalart-Allmaras model is observed to perform better near the back suction side, downstream of the shock impingement.

2.4 Conclusions

A RANS solver is implemented with different turbulence models: the one-equation model of Spalart-Allmaras [11], the two-equation SST k-ω model of Menter [12], the k-ϵ model with the Chien's damping functions [14], and the four-equation model k-ϵ-v^2-f proposed by Durbin [15]. All show good agreement with experimental and theoretical data with the flow on a flat plate.

This section has for objective to evaluate different turbulence models for turbomachinery application. A novel five-block topology is developed to control the grid refinement around the blade, in the throat passage, and in the wake area of a transonic turbine vane. The computation of the turbulent flow around this turbine vane case is possible for the Spalart-Allmaras model and the k-ϵ model, but encounters the occurrence of negative turbulence variables just downstream of the trailing edge with the k-ϵ-v^2-f model.

Despite considerable enhancements in the prediction of selected separated flows,

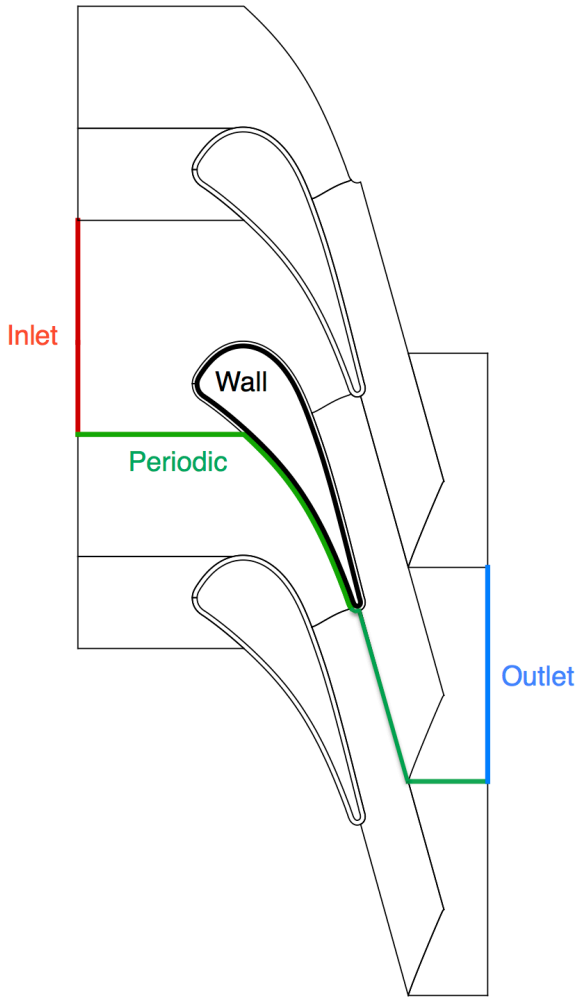

Figure 2.3: Multi-block topology and boundary conditions for turbine case

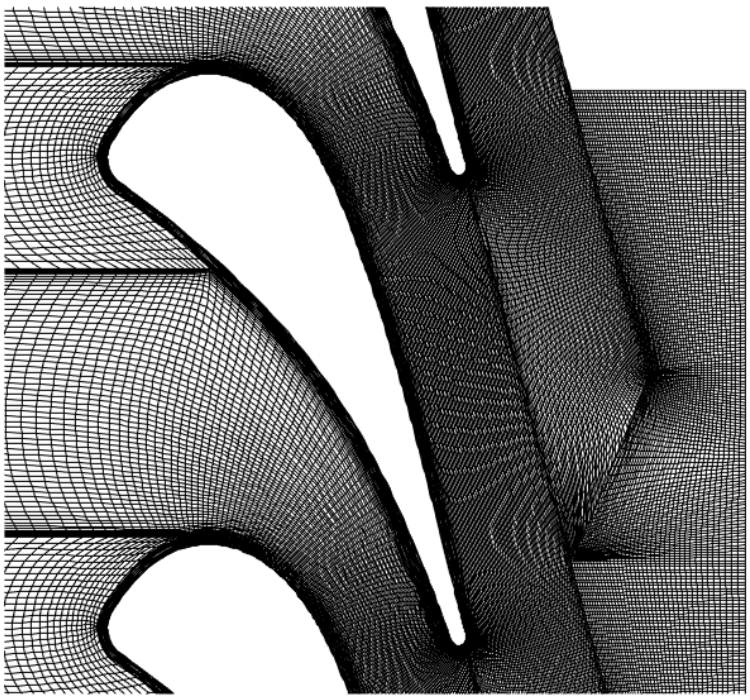

Figure 2.4: O-Grid around high-pressure turbine

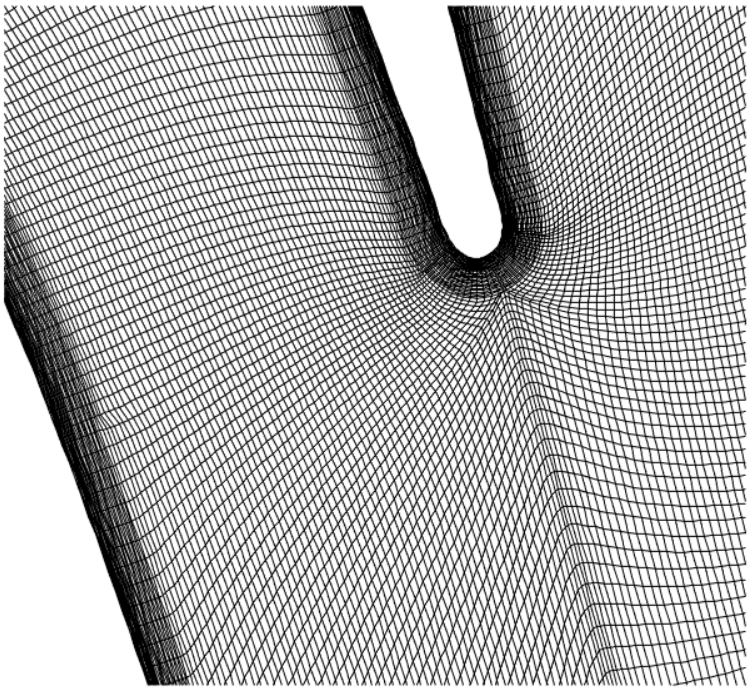

Figure 2.5: Grid refinement in throat area of high-pressure turbine

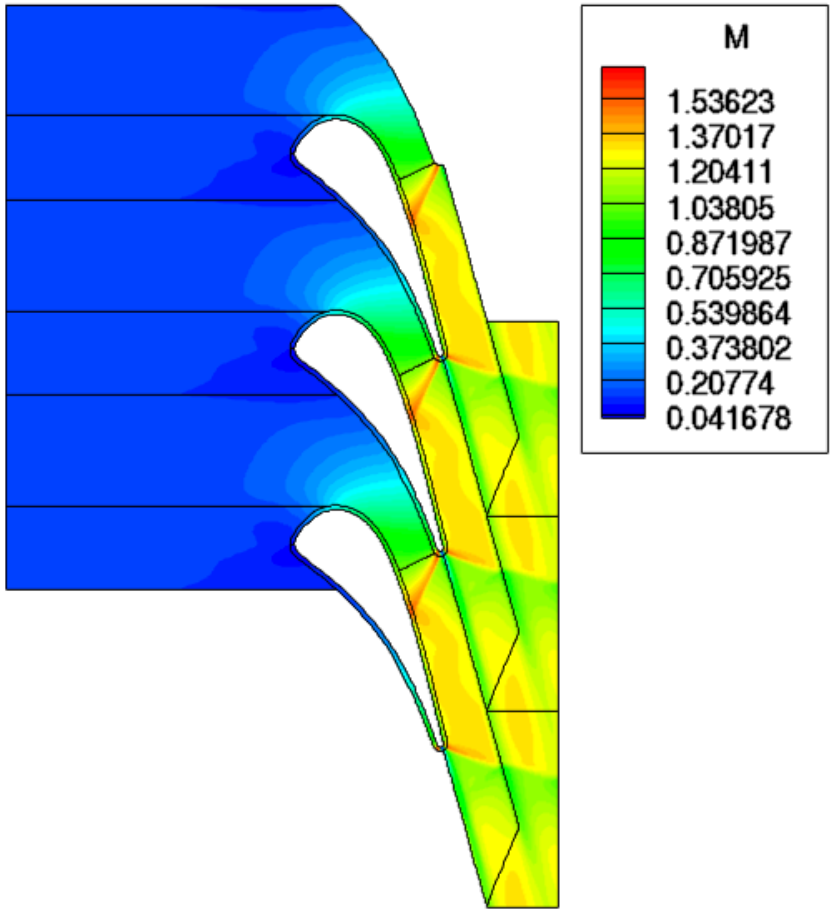

Figure 2.6: Mach number field, M_{is}=1.2 at the outlet, Spalart-Allmaras

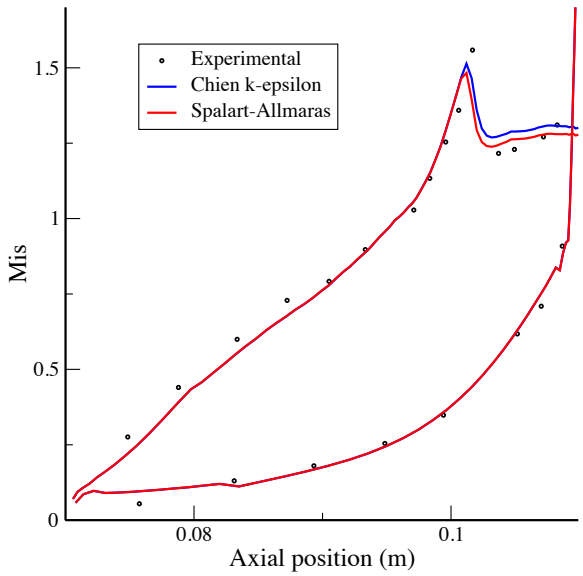

Figure 2.7: Isentropic Mach number on blade, M_{is}=1.2 at the outlet

the literature also acknowledges numerical instabilities and difficult convergence of the k-ϵ-v^2-f turbulence model [16, 18, 19, 20]. Recommendations for alternative approaches to evaluate the four-equation turbulence model on turbomachinery applications are two-fold. A first option would be to compute the flow with an implicit solver, which may help with stability. A second option would be to consider more recent versions of the four equation model. Both the k-ϵ-ζ-f version [18] and the k-ϵ-φ-α version [20] have reported enhanced numerical robustness.

3. ATTENUATION OF UNSTEADY SHOCK INTERACTION IN HIGH-PRESSURE TURBINES*

This chapter presents the method and the results related to the second objective of the dissertation, i.e. the attenuation of unsteady shock interaction in high-pressure turbines.

3.1 Introduction

3.1.1 Shock interaction in high-pressure turbines

In the development of any modern aeroengine, the high-pressure turbine operates in harsh environment (high temperatures downstream of the combustor and mechanical solicitations). Higher loading per row allows to reduce the number of stages, limiting the weight of the machine. It contributes therefore to lower the fuel consumption of commercial aircrafts. However, an increase of load implies that the flow across the turbine passages is transonic, resulting in shock-wave interactions [21]. Denton et al. [22] describes the aerodynamics of the trailing-edge shock system within transonic turbine vanes. The vane shocks waves travel downstream, impacting periodically on the rotor blades (See Fig. 3.1). Giles [23] identified the sweeping of the direct shock from the crown of the rotor blade towards the leading edge, causing variations in the rotor lift of 40% of the mean level. The downstream rotor is therefore prone to suffer from high cycle mechanical and thermal fatigue.

Attempts to mitigate the unsteady vane-rotor shock interaction could be classified into improved designs through a better physical understanding [24, 25, 26, 27], ac-

*Reprinted with permission from "Differential evolution based soft optimization to attenuate vane-rotor shock interaction in high-pressure turbines" by Joly, M. M. Verstraete T. and Paniagua G., *Applied Soft Computing*, Vol. 13, No. 4, 2013, pp. 1882–1891, Copyright 2013 by Elsevier.

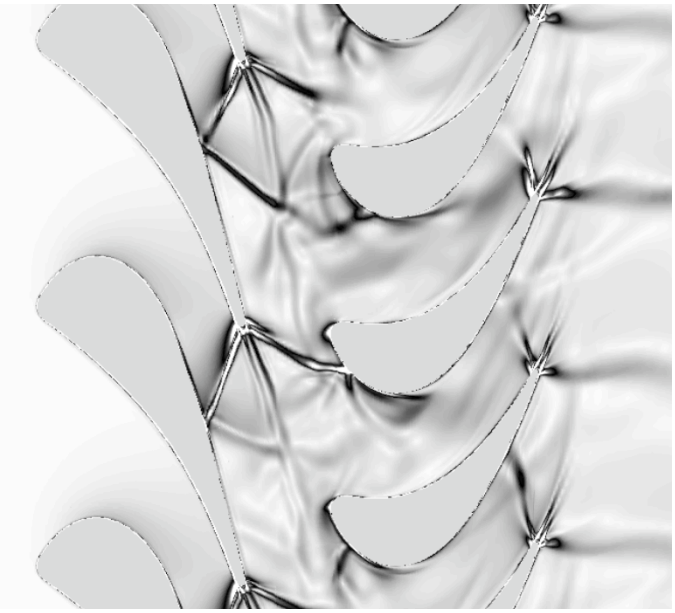

Figure 3.1: Vane/Rotor shock interaction

tive control systems [28], and numerical optimizations with neural networks [29, 30]. Unsteady turbine stage computations with high-fidelity are however extremely expensive and their implementation together with optimization algorithms is limited to 2D profiles. The unsteady optimization of real 3D geometries remains unpractical with modern computers, even with the assistance of surrogate models. The present research proposes alternatively a soft computing methodology based on evolutionary optimization, and considers robust, accurate, and computationally affordable evaluations to redesign the vane, with the ultimate goal to limit the unsteady vane-rotor shock interaction.

3.1.2 Approach to mitigate unsteady forcing on rotor

It is proposed to modulate directly the pitch-wise static pressure distribution downstream of the stand-alone vane with Reynolds-Averaged Navier-Stokes (RANS) computations, as suggested by Shelton et al. [31]. The aim is to attenuate the

strength of the shock waves that propagates downstream of the vane. The soft optimization is expressed as a multi-objective problem. A Differential Evolution (DE) algorithm is used and assessed on mathematical test cases. For the vane design a parameterization of the two-dimensional section is developed with particular focus on the contraction channel. Another parameterization of the stacking line allows to introduce lean of the three-dimensional geometry. Each candidate is processed by an automatic structured mesh generator and evaluated by Navier-Stokes computations. In the result sections, the obtained optimal two- and three-dimensional vane geometries are presented. Their flow features are analyzed to understand how the optimized geometry reduces the downstream propagation of shock waves. Subsequently to the vane optimization, the abatement in the rotor forcing was quantified using an unsteady solver based on a Non-Linear Harmonic (NLH) method [32].

3.2 Soft optimization methodology

3.2.1 A multi-objective optimization problem

3.2.1.1 Concurrent objectives

The optimization of the stand-alone vane has two objectives. The first objective is to minimize the distortion of the pitch-wise static pressure at the vane outlet. Figure 3.2 displays the location where the pressure is evaluated, 35% of the axial chord downstream of the vane trailing edge. The distortion downstream of the vane is assessed by the standard deviation along the pitch-wise direction, expressed by equation 3.1.

$$\sigma = \sqrt{\int_{y_0}^{y_0+pitch} \frac{(p(1.35 * \lambda, y) - \bar{p})^2}{pitch} dy} \tag{3.1}$$

The second objective is to ensure high efficiency. Therefore the kinematic loss

coefficient (equation 3.2) ought to be minimized.

$$\xi = 1 - \eta = 1 - \frac{V_2^2}{V_{2is}^2} \tag{3.2}$$

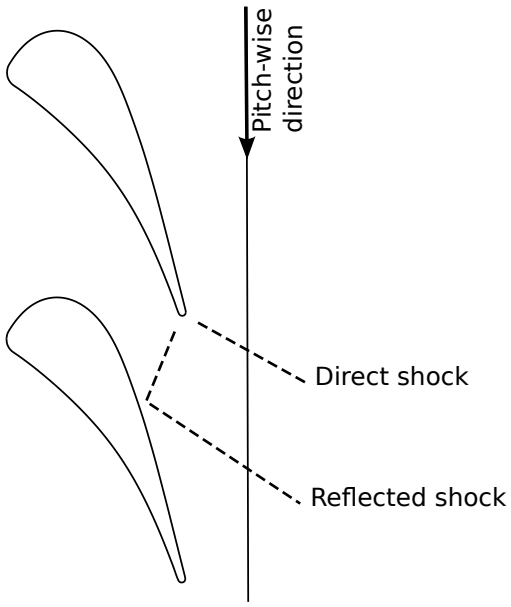

Figure 3.2: Plane of interest to assess vane downstream distortion

3.2.1.2 Optimization algorithm

The DE/rand/1/bin algorithm of Price and Storn [33], a scheme widely used in the literature [34], is employed. The selection procedure is modified following the approach of Madavan [35], which extends the basic algorithm to multi-objective problems incorporating the non-dominated sorting and ranking selection scheme of Deb et al. [36]. The selection procedure favors the designs that are close to the target vector in order to preserve the localized search capacities of the classical DE scheme for single objective problems. In his paper, Madavan reported that the method is

self-adaptive, elitist, and capable to maintain diversity in the Pareto set.

Two two-dimensional mathematical optimization problems are used to verify the correct implementation of the method for the current research. The first exhibits a discontinuous objective space and is formulated as follows.

$$\begin{aligned} \text{Minimize} \quad & f_1(\vec{x}) = 5sin(\pi x_1) + cos(\pi x_2) \\ & f_2(\vec{x}) = sin(\pi x_1)cos(\pi x_2) + x_1 x_2 \\ \text{Subject to} \quad & -1 \leqslant x_1 \leqslant 1 \\ & -1 \leqslant x_2 \leqslant 1 \end{aligned}$$

The constants used by the DE algorithm are $F = 0.3$ and $C = 0.8$. The optimization problem results into a discontinuous Pareto front expressed with equations 3.3 and 3.4.

$$f_2 = -\frac{f_1 + 1}{5} + \frac{1}{\pi} asin\left(\frac{f_1 + 1}{5}\right) - 1 \tag{3.3}$$

$$f_2 = -f_1 - 5 - \frac{1}{2\pi} acos\left(f_1 + 5\right) \tag{3.4}$$

The second test problem is the ZDT3 function, which comprises multiple local optima. It has two objectives, expressed with equations 3.5, 3.6 and 3.7, with 30 variables bounded in the range $[0; 1]$.

$$f_1(\vec{x}) = x_1 \tag{3.5}$$

$$f_2(\vec{x}) = g(\vec{x}) * \left[1 - \sqrt{\frac{x_1}{g(\vec{x})}} - \frac{x_1}{g(\vec{x})} * sin(10 * \pi * x_1)\right] \tag{3.6}$$

$$g(\vec{x}) = 1 + \frac{9}{n-1} * \sum_{i=2}^{n} x_i \tag{3.7}$$

Figures 3.3 and 3.4 shows results for the two problems. Convergence is obtained after 20 generations of populations of 30 individuals and after 300 generations with

a population size of 40 individuals, for the first and second problem respectively. In both cases, optimal individuals are well distributed all along a Pareto front. The algorithm is therefore capable to converge while offering diversity among the non-dominated solutions.

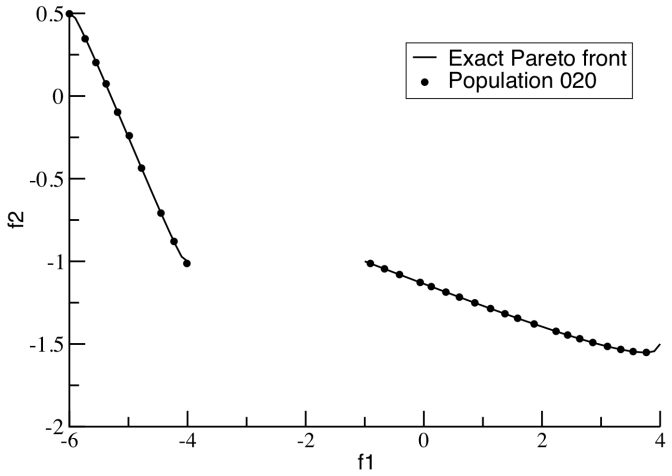

Figure 3.3: First optimization test case

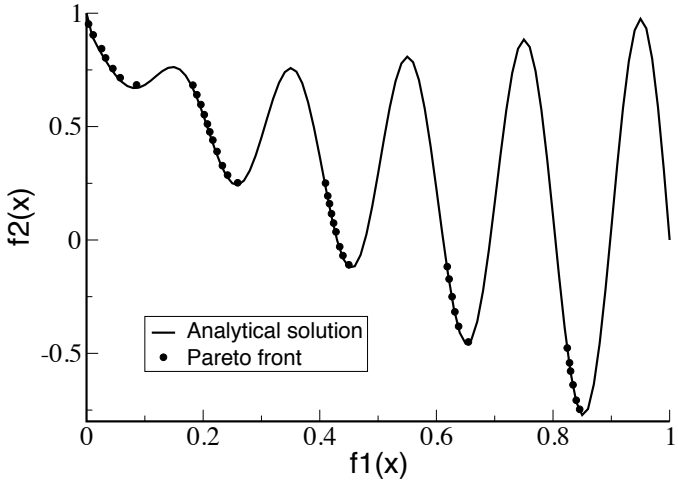

Figure 3.4: ZDT3 optimization test case

3.2.2 Optimization of vane contraction channel

The parameterization is a crucial step in any optimization problem, since it defines how an optimal geometry can be represented. Each parameter, i.e. element of the design vector $\mathbf{x}$, should have a clear impact on the geometry definition to ease the identification of the optimal set of parameters. Moreover, the design space, defined by ranges for each parameter, accounts for the available shape variety; if the optimal shape cannot be represented, it will not be found by the optimizer.

3.2.2.1 Two-dimensional section parameterization

Two-dimensional airfoil sections are defined for each height (along the radial direction), starting from the definition of the camberline by the following set of parameters: axial chord λ, stagger angle γ, inlet metal angle β_{in} and outlet metal angle β_{out} (see Fig. 3.5 left). The stagger angle and axial chord length define the position of the leading edge and trailing edge. The intersection of the inlet and outlet lines respecting the inlet and outlet angle defines the point P_{Mid} shown on Fig. 3.5 (left). The vertex P_{LE}, P_{Mid} and P_{TE} define the control points of the Bézier curve describing the camber line.

The suction and pressure side curves are also defined by Bézier curves, whose control points are specified relative to the camber line. In Fig. 3.5 (right) the construction of the suction side curve is illustrated. First a stretching law is imposed on the camberline curve. For each point excepting the first and the last two ones, a normal distance is specified to position a control point. For the first point the distance is computed by a specified radius of curvature ρ_{LE}, allowing geometric continuity in the second derivative at the leading edge between the suction side and pressure side curve. The distance to the last point is equal to the trailing edge radius ρ_{TE}, which is also specified. Finally, the second last control point is computed by a specified

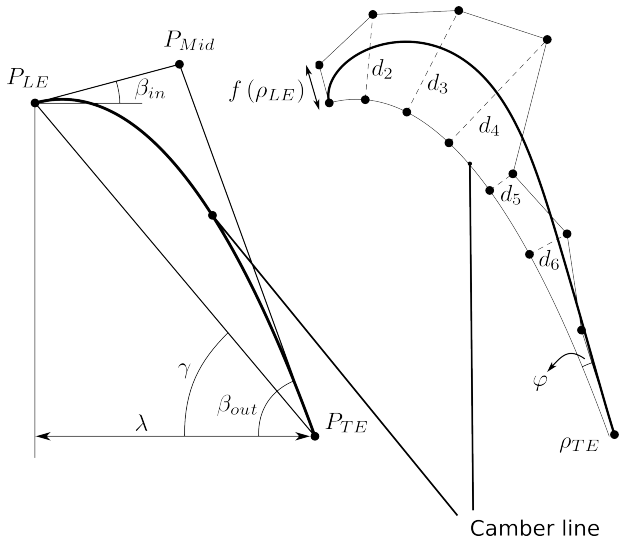

Figure 3.5: Construction of camberline (left) and suction side (right) of a 2D section profile

wedge angle φ, see Fig. 3.5 (right).

A large design space is required to maximize the available shape variety and therefore the capacity to represent the optimal shape. This could generate non-physical profiles with negative or too large thickness resulting in the overlapping of airfoil geometries, blocking the passage to the flow. A geometry filter is therefore implemented to exclude such unfeasible geometries, based on an analysis of the parameters set. From the control points set and the corresponding curves, crossings of suction and pressure sides are detected to prevent negative thickness. Also, the computation of the minimal distance between the suction side with the adjacent blade pressure side avoids too narrow flow paths. This check is performed before each performance evaluation, to bypass the Navier-Stokes computation in case of a negative judgement.

High-pressure turbines are characterized by the passage ducted by two adjacent airfoils. This parametrization allows a detailed control of the throat region (See Fig. 3.6, left). To be integrated in the optimization process, the mesh generation is

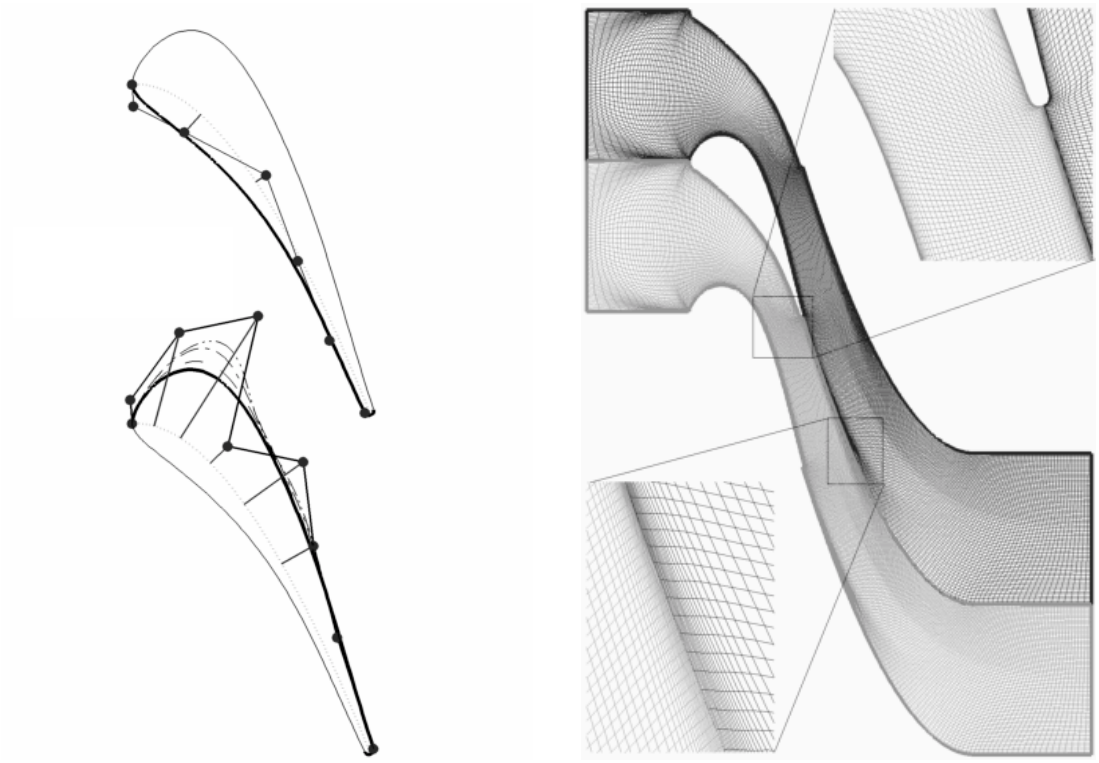

Figure 3.6: Contraction channel parameterization (left), 2D mesh (right)

parametrized to be executed in an automated manner. A H-type periodic mesh (see Fig. 3.6, right) is used and particular care is addressed to the meshing of the throat area and the non-matching periodic boundaries.

3.2.2.2 Three-dimensional vane parameterization

Three-dimensional annular vane geometries are generated from the stacking of several sections at different heights (along the radial direction). A stacking law defines the relative circumferential position of the leading edge for each section, introducing lean to the 3D vane. This law is defined by a Bézier curve with 3 degrees of freedom depicted in Fig. 3.7, left: tangent angle at the hub (alpha1), tangent angle at the tip (aplha2), circumferential position of the tip leading-edge relative to the

hub one (xtip). From this law, the positions of 5 radially equally spaced sections are extracted. The individual 2D sections are connected by a smooth surface and finally a 3D mesh is generated based on this airfoil definition (Fig. 3.7, right).

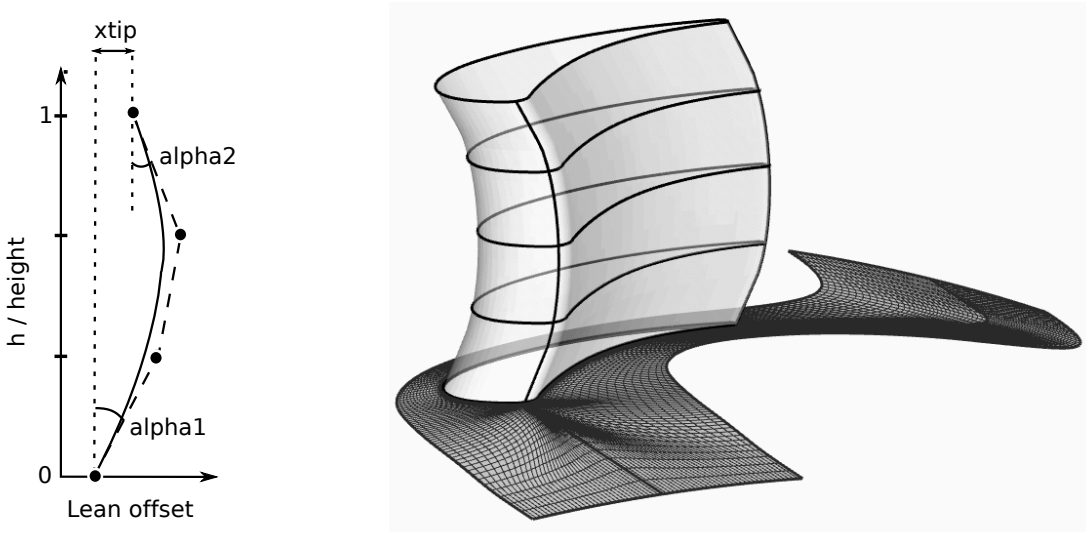

Figure 3.7: Stacking line parametrization (left), geometry and mesh (right)

3.2.2.3 Performance evaluation

The aerodynamic performance of each design candidate is evaluated with the code TRAF [37]. The Reynolds-Averaged Navier-Stokes equations are solved using a Runge-Kutta time integration and a discretization based on finite volume with a cell-centered scheme. The Baldwin and Lomax turbulence model is chosen; it is fast and also known to be robust in turbomachinery applications with attached flows [38]. Moreover, a good match with experiments has been obtained. Figure 3.8 shows good agreement with experimental data on the isentropic Mach number distribution around the baseline airfoil at mid-span [27].

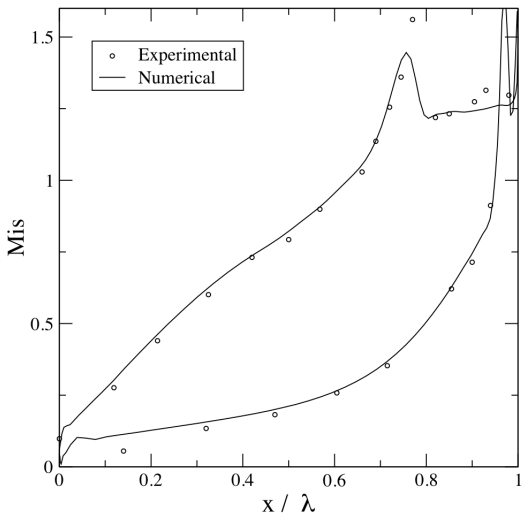

Figure 3.8: Mach number distribution at mid-span for baseline

3.3 Optimization of stand-alone vane

The Differential Evolution algorithm is applied to redesign the stand-alone vane to reduce its downstream distortion and minimize its losses. The optimization is first performed on the 2D profile at mid-span and subsequently on the full 3D design.

3.3.1 Two-dimensional vane optimization

The 2D design of vane sections should comply with the 1D turbine flow field resulting from a through-flow computation. In the present turbine case, the flow conditions at mid-span are the following:

- Inlet total pressure, $P_{01} = 162000$ Pa
- Inlet total temperature, $T_{01} = 440$ K
- Inlet flow angle, $\alpha_1 = 0$ deg.
- Outlet flow angle, $\alpha_2 = 74.7$ deg.
- Outlet isentropic Mach number, $M_{2is} = 1.2$

The geometry requirements to respect are:

- Axial chord, $\lambda = 0.0411$ m
- Stagger angle = 53.9 deg.
- Pitch/λ at mid-span = 1.3128
- Trailing edge diameter = 2mm

The stagger line, defined by the axial chord and the stagger angle, is set to be the same as the baseline, whose coordinates were published by Sieverding et al. [39]. The airfoil number and end-walls radii fix the pitch for 2D sections. Finally, the trailing edge thickness is defined to allow coolant ejection. The shape is imposed to be semicircular to ease fabrication.

The design space includes 14 parameters, which are summarized in Table 3.1. Section 3.2.2.1 described how the parameters and the definition of the suction and pressure sides relate.

Parameter	Lower limit	Upper limit
SS Ctrl Pnt 1,2,3 (*Cax)	0	0.7
SS Ctrl Pnt 4 (*Cax)	-0.1	0.5
SS Ctrl Pnt 5 (*Cax)	0	0.4
PS Ctrl Pnt 1 (*Cax)	-0.1	0.5
PS Ctrl Pnt 2 (*Cax)	-0.1	0.4
PS Ctrl Pnt 3,4 (*Cax)	-0.1	0.3
StaggerAngle (deg)	-60	-50
BetaInlet (deg)	-20	15
BetaOutlet (deg)	-80	-60
Wedge Angle SS, PS (deg)	1	30

Table 3.1: Design space for 2D optimization

3.3.1.1 Single-point optimization

The objective of minimal downstream distortion is considered (equation 3.1). The loss coefficient (equation 3.2) and mass flow are constrained to be lower and higher than the baseline values, respectively. Acceptable values of the outlet flow angle are considered within the range of 74.7 $\pm$0.5 deg.

An optimization run with 200 generations of 60 individuals is performed and the evolution of the process is illustrated in Figure 3.9. Through the optimization process, the individuals of each population are progressively satisfying the constraints. Hereafter the objective value is minimized, leading finally to a 43.2% attenuation of the downstream distortion. Each evaluation taking 2 minutes of CPU time, the whole optimization runs for about 10 hours on 40 processors.

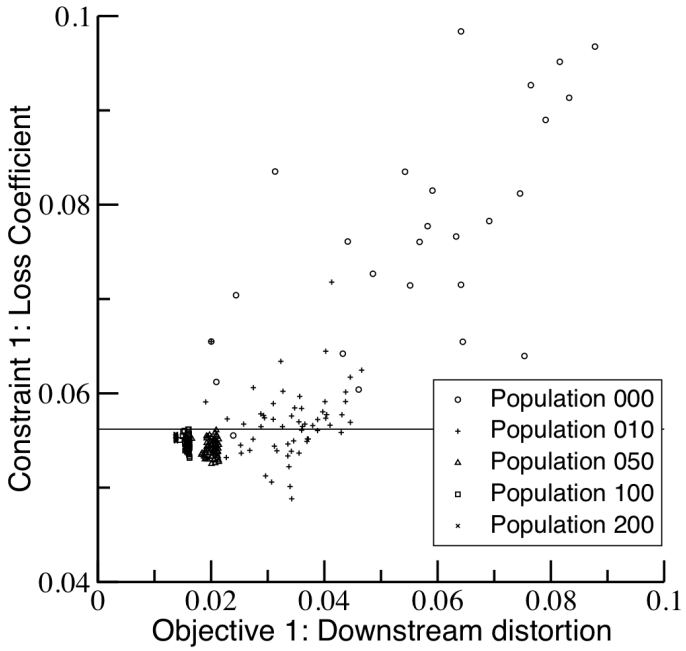

Figure 3.9: Optimization iterations for single-point strategy

3.3.1.2 Multi-point optimization

The previous optimization successfully addresses the objective of reducing the downstream distortion while preserving the losses at design conditions. However, it does not consider off-design conditions.

A multi-point optimization is therefore performed with three objectives:

- reduce the downstream static pressure distortion (Eq.1) at nominal condition, M_{2is}=1.2
- reduce the losses at nominal condition, M_{2is}=1.2
- reduce the losses at off-design condition, M_{2is}=0.8

After 200 generations of 60 individuals, the Pareto front of the multi-objective strategy includes the single-objective optimum (See Figure 3.10). The projection of the Pareto front on the off-design losses/downstream distortion plane (See Figure 3.10, bottom) highlights a large increase of losses at off-design condition for individuals that provide great attenuation of downstream distortion. It is still possible to find a trade-off with equivalent losses at design and off-design points with a slightly reduced downstream distortion, compared to the baseline. However, within the present work, priority is set to a large attenuation of downstream distortion, sacrificing the loss at off-design. As such, the single-objective optimum is considered for the following analysis.

3.3.1.3 Optimal 2D profile at mid-span

The best candidate obtained with the single-point strategy provides a reduction of 43.2% of the downstream pitch-wise static pressure standard deviation. The loss coefficient at the design point is 1.4% lower than the baseline, the outlet flow angle 0.02 degree larger and the mass flow increased by 0.3%.

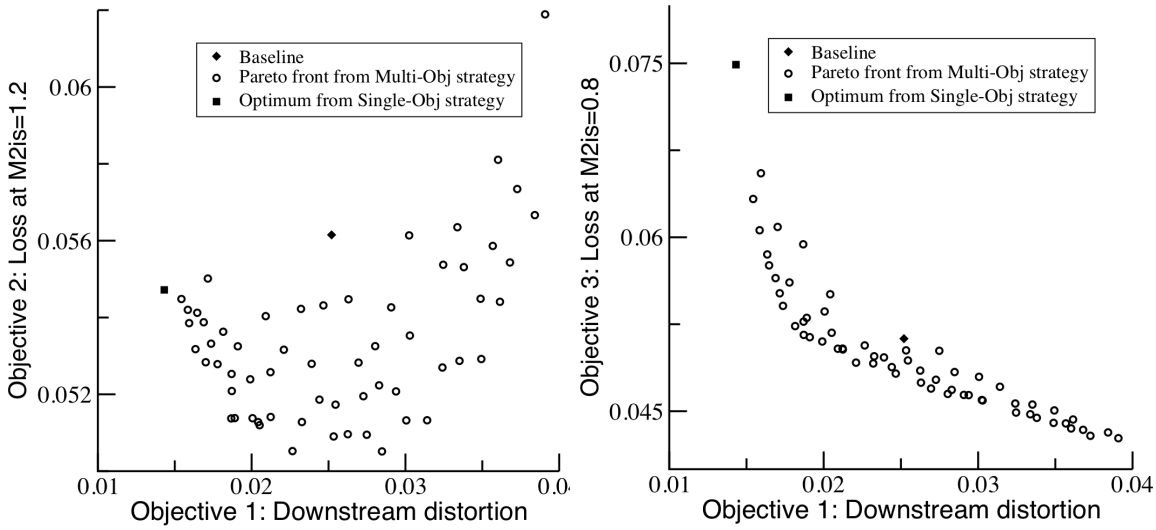

Figure 3.10: Pareto front of multi-point strategy, downstream distortion V.S. loss at design point (left), downstream distortion V.S. loss at off-design (right)

It can be observed that the parametrization requires a large design space to produce the desired airfoil, with one control point of the suction side reaching till the pressure side (Figure 3.11). The corresponding shape variety enables a larger thickness on the pressure side with a similar suction side compared to the baseline. The downstream pitch-wise static pressure distribution (Fig. 3.12, left) shows a clear reduction of the direct shock strength at y/λ=-4,1. The reflected shock (y/λ=-4.6) is however slightly stronger. Density gradient fields confirm this observation (See Figure 3.13). The left running shock, i.e. direct shock, clearly appears with lower intensity for the optimized airfoil. By contrast, the right running shock has a stronger intensity than the baseline, also revealed by the higher inclination of the oblique shock. Its reflection on the adjacent vane suction side, i.e. reflected shock, appears with higher intensity. A strong impingement on the suction side of the adjacent vane is also observed on the Mach number distribution (See Figure 3.12, right).

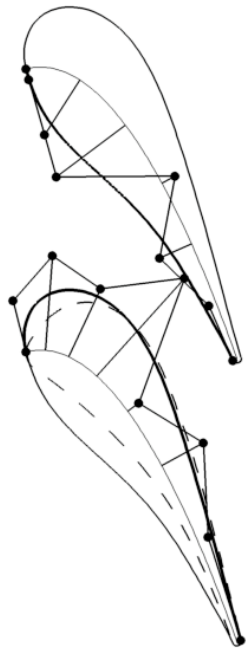

Figure 3.11: Optimal vane geometry for single-point strategy

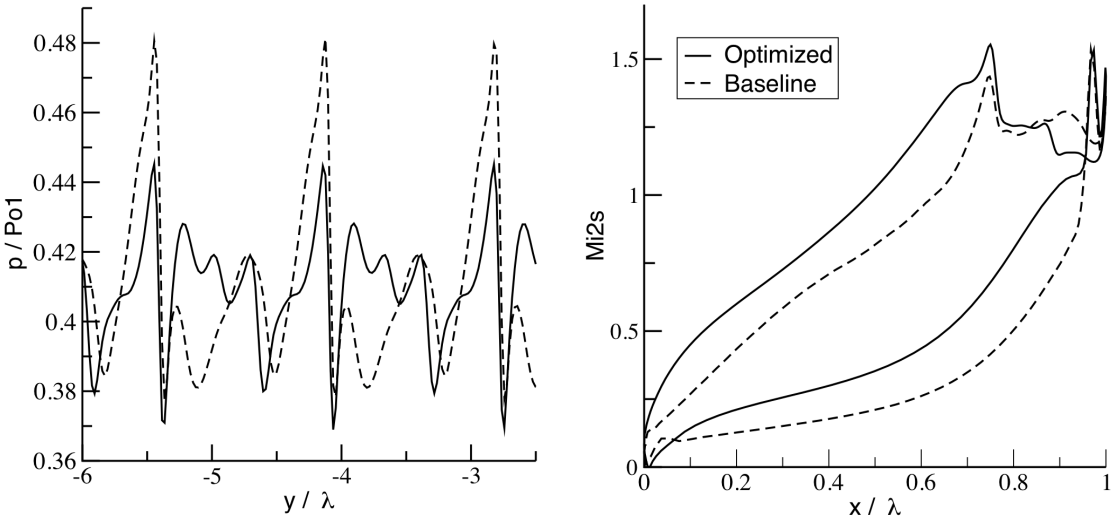

Figure 3.12: Optimal vane for single-point strategy, downstream distortion (left), Mach number distribution (right)

With a similar suction side and increased thickness on the pressure side, the contraction channel of the optimized airfoil is narrower than the baseline's. The channels are choked and therefore sonic sections impose the mass flows. For the baseline, the sonic section is located at the end of the convergent channel and coincides with the geometric throat, a line from the pressure side trailing edge to the suction side (Fig. 3.13, red lines). On the other hand, the channel resulting from the optimized airfoil is convergent-divergent. The sonic section moved upstream and appears inclined. The convergent-divergent shape of the optimized contraction channel over-accelerates the flow downstream of the sonic line, increasing the Mach number levels on the rear pressure side and mid suction side (Fig. 3.12, right). With a faster flow within the contraction channel, the trailing edge shock system is modified and the propagation of shock waves downstream is remarkably attenuated.

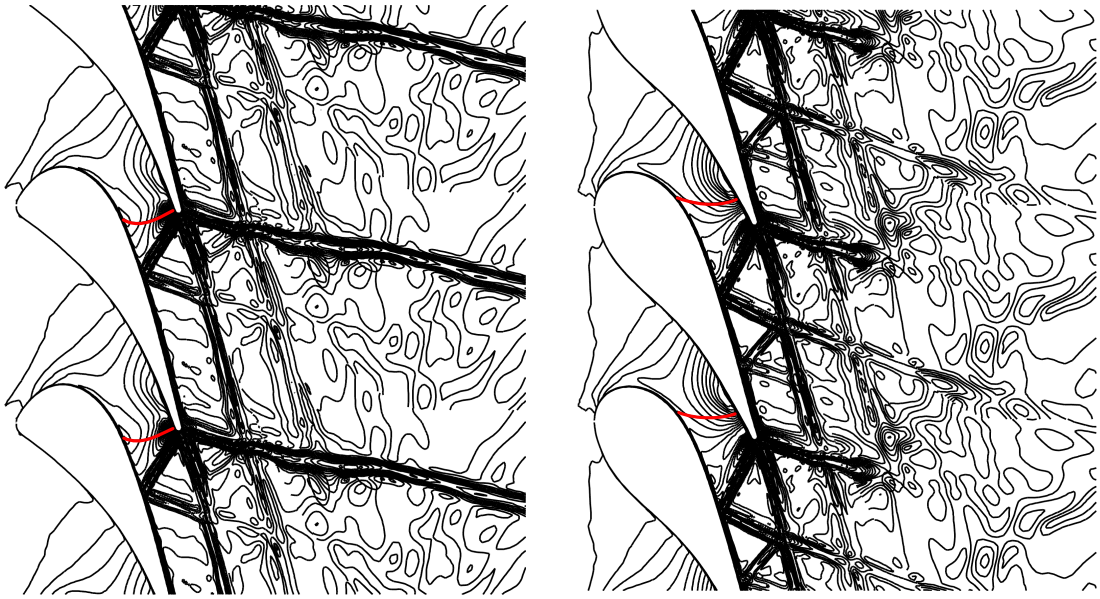

Figure 3.13: Density gradients fields (black) and sonic lines (red) for baseline (left) and optimized (right) geometries

Transonic airfoil correlations, such as the one proposed by Sieverding [24], indicated that higher wedge angles would result in lower losses. The obtained optimal geometry presents larger thickness on the pressure side compared to the baseline, resulting in a greater trailing edge wedge. Consequently, a positive effect on the losses could be expected from the correlation. A contradiction still remains with other correlations quoting larger losses in convergent-divergent passages. The authors believe that the present optimization techniques revealed an unprecedented geometry that correlations from the published literature did not allow to investigate. The obtained combination of a convergent-divergent contraction channel with large trailing edge wedge angle and straight rear suction side enables to reduce the downstream propagation of shock waves emanating from the trailing edge shock system, while preserving low losses.

3.3.2 Radial stacking of optimal 2D section at mid-span

The 2D section optimized at mid-span is stacked radially along the leading edge to evaluate the potential of 2D section optimization in improving the 3D performances. The resulting airfoil is cylindrical and provides a reduction of downstream distortion of 40.4% compared to the baseline, with similar average outlet flow angle (-0.05 degree) and mass flow (+0.6%). However, the efficiency is lower, with the kinematic loss increased by 8.05%. This is a consequence of the radial stacking of the optimized 2D section at mid-span, which provides non-optimal sections at lower and upper span. A multi-row computation confirms a decrease in stage efficiency from 91.44% for the baseline to 90.97% (-0.56%) for the radial stacking of 2D optimized section at mid-span.

3.3.3 Three-dimensional vane optimization

In the quest to further improve the downstream distortion while preserving a high efficiency, a three-dimensional optimization is performed. The flow conditions of the annular vane are:

- Inlet total pressure, $P_{01} = 162000$ Pa
- Inlet total temperature, $T_{01} = 440$ K
- Inlet flow angle, $\alpha_1 = 0$ deg.
- Outlet flow angle, $\alpha_2 = 74.0$ deg.
- Outlet isentropic Mach number, $M_{2is} = 1{,}2$

The geometry requirements are:

- Axial chord, $\lambda = 0.041163$ m
- Stagger angle = 53.9 deg.
- Radius at hub and tip, $R_{hub} = 0.334$m, $R_{tip} = 0.395$m
- Trailing edge radius = 2mm

This 45-parameters optimization includes 3 parameters (see Table 3.2) for the lean and 14 parameters (see Table 3.1) for each of the three adaptable sections at

Parameter	Lower limit	Upper limit
Alpha angle at hub (deg)	-30	30
Alpha angle at tip (deg)	-30	30
Xtip (*Cax)	-0.3	0.3

Table 3.2: Design space for lean in 3D optimization

hub, mid-span and tip. The complexity of the 3D design arises from the large number of parameters. They enable one to vary the airfoil profiles along the span and to introduce curvature in the stacking of these different profiles. It is crucial to allow such degrees of freedom in the geometry generation, because the flow around turbines comprises important 3D patterns, such as secondary flows and end-wall effects.

3.3.3.1 Optimal 3D vane

An optimization run is performed with the objective of minimal downstream pressure distortion and several constraints. The standard deviation of the downstream static pressure along the pitch-wise direction is evaluated at each height (from 1 to N) using equation 3.1. The average distortion along the span height is evaluated using equation 3.8.

The loss coefficient and mass flow are constrained to be lower and higher than the baseline values, respectively. Acceptable levels of outlet flow angle are considered within the range of 74.0 $\pm$0.5 deg.

$$\sigma = \frac{1}{N}\sum_{i=1}^{N}\sqrt{\int_{y_0}^{y_0+pitch}\frac{(p(1.35*\lambda,y)-\bar{p})^2}{pitch}dy} \tag{3.8}$$

The optimization consists in 40 iterations of 60 individuals and its process is shown in Figure 3.14). Each evaluation consuming about 1 hour of CPU time, the whole optimization costs about 40 hours on 40 processors.

The downstream distortion is attenuated by 56.1% with all constraints fully respected. The outlet flow angle (-0.38 deg.) is similar to the baseline and the mass flow slightly larger (+3.5%). The kinematic loss is reduced (-0.4%), leading to a very similar stage efficiency of 91.37% (-0.07%). Therefore the 3D optimization with lean and section adaptation enables a further improvement in downstream distortion,

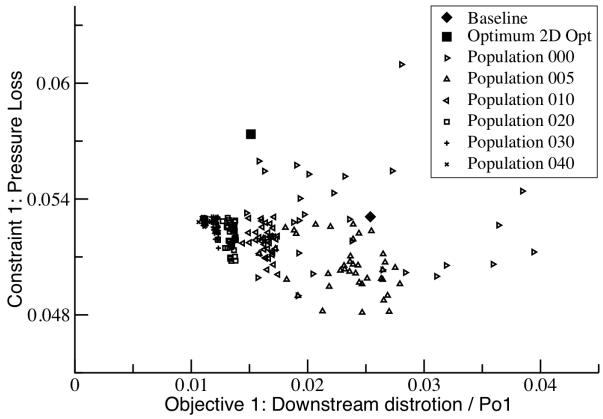

Figure 3.14: Optimization iterations for 3D design

while offering similar efficiency compared to the baseline.

The comparison of density gradients fields downstream of the vane between the baseline, the 2D optimum and the 3D optimum (Fig. 3.15) shows a clear reduction of the direct shock. It is completely attenuated above mid-span with the 2D optimum. Its strength is reduced at lower spans, but the reflected shock appears then stronger. The 3D optimum enables eventually to reduce drastically the strength of both shocks.

Fig. 3.16 highlights a large decrease of the downstream distortion along the whole span. The losses are increased close in the tip region, but largely decreased around the mid-span. Mass flow and outlet flow angle distributions present larger and similar average values along the span compared to the baseline, respectively.

3.4 Unsteady vane-rotor interaction assessment

Subsequently to the vane optimization, the unsteady forcing on the rotor downstream of the optimal vane is computed. The aim is to assess the attenuation of vane-rotor interaction obtained with the redesign of the vane.

A non-linear harmonic approach is used to compute the unsteady flow field in the stage (vane and rotor). This method was first introduced by He et al. [40]

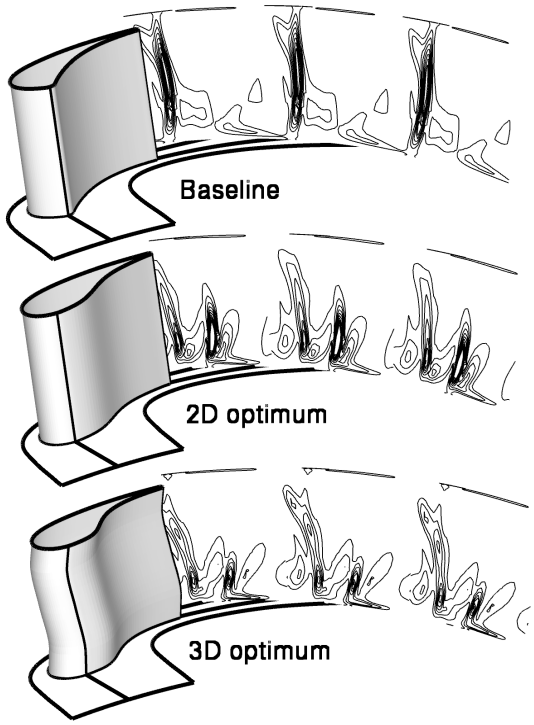

Figure 3.15: Geometry and density gradient fields downstream at x=1.35*Cax, baseline (up), radial stacking of 2D optimum (mid), 3D optimum (bottom)

and has been integrated in the code FineTurbo of Numeca International [32]. The flow is decomposed into a time averaged field and periodic unsteady perturbations around the mean flow field. The unsteady components are estimated by means of the Fourier decomposition of the periodic fluctuations and conservation laws for each harmonic are solved in the frequency domain. The grid has a multi-block topology and the Baldwin Lomax turbulence model is used. Comparisons with 3 harmonics show relatively good agreement with experimental results (See Fig. 3.17), especially on the axial forcing.

Unsteady forcing on the rotor are extracted at 3 radial positions (10%, 50% and 90% of the blade height). The axial and tangential forces are computed along a rotor

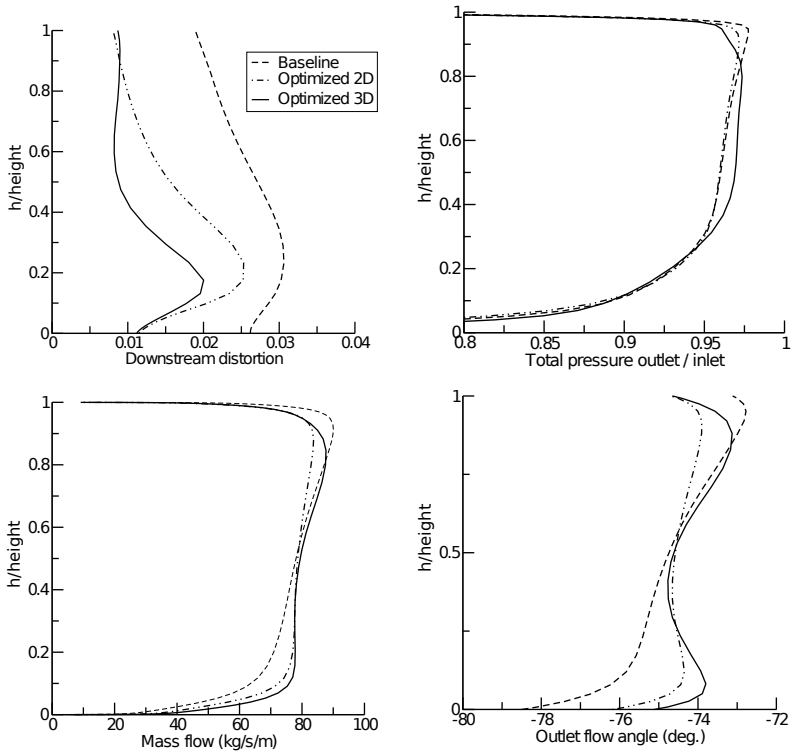

Figure 3.16: Downstream distortion (top-left), mass flow (bottom-left), total pressure losses (top-right) and outlet flow angle (bottom-right) distributions along the span downstream of the 3D optimized vane

pitch (Fig. 3.18). Amplitude and standard deviation are summarized in Tables 3.3 and 3.4, on the rotor downstream of the 2D and 3D optimized vanes respectively. The forcing on the rotor is considerably attenuated, with a largest decrease of 61% at mid-span downstream of the 3D optimal design. This results confirm the reduction in high-cycle fatigue risk.

3.5 Conclusions

Unsteady turbine stage computations with high-fidelity Navier-Stokes solvers (such as URANS, LES, DES) remain extremely expensive with modern computers and their implementation together with optimization algorithms is unpractical.

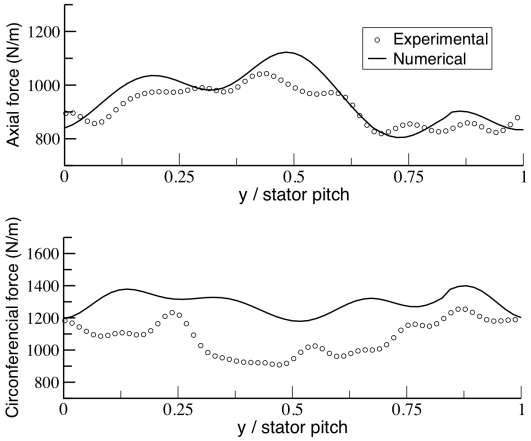

Figure 3.17: Validation of non-linear method, unsteady forcing at 85% of the span

	Amplitude	Standard deviation
$F_{ax}at90\%$	-22.1%	-25.1%
$F_{tan}at90\%$	-41.0%	-46.6%
$F_{ax}at50\%$	-54.8%	-54.3%
$F_{tan}at50\%$	-19.3%	-22.8%
$F_{ax}at10\%$	-19.7%	-22.4%
$F_{tan}at10\%$	-13.5%	-18.1%

Table 3.3: Rotor unsteady forcing at 10%, 50% and 90% of the blade height downstream of the 2D optimal vane compared to the baseline

	Amplitude	Standard deviation
$F_{ax}at90\%$	-35.3%	-33.2%
$F_{tan}at90\%$	-19.1%	-18.9%
$F_{ax}at50\%$	-61.0%	-57.7%
$F_{tan}at50\%$	-52.8%	-58.4%
$F_{ax}at10\%$	+0.9%	-4.8%
$F_{tan}at10\%$	-28.4%	-24.3%

Table 3.4: Unsteady forcing on the rotor at 10%, 50% and 90% of the blade height downstream of the 3D optimal vane compared to the baseline

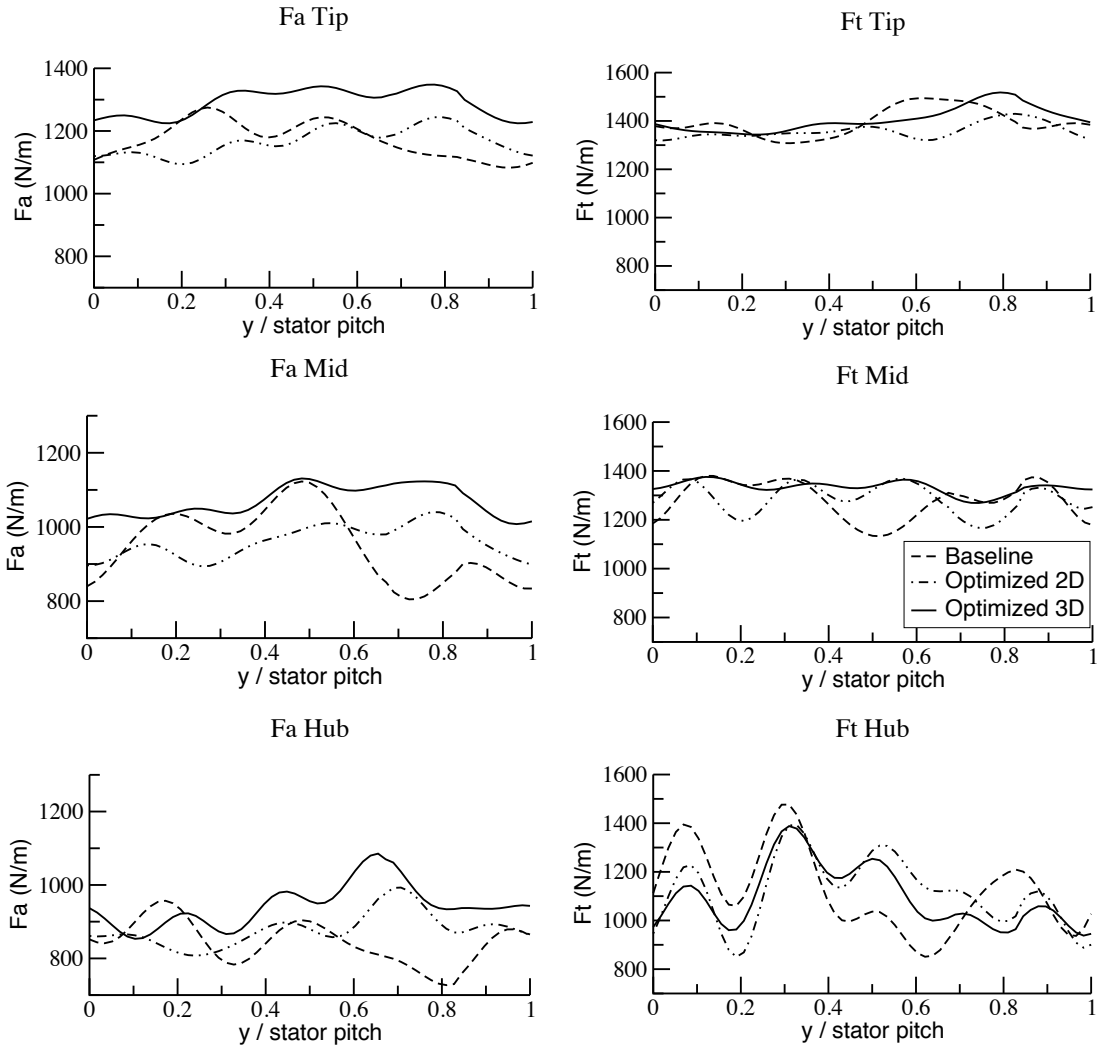

Figure 3.18: Unsteady forcing on the rotor downstream of the 2D and 3D optimized vanes, axial force (left) and tangential force (right), at 90% (top), 50% (mid), 10% (bottom) of the span

The present research proposes a soft computing methodology to reduce the unsteady forcing in high-pressure transonic turbines. It consists of an evolutionary optimization based on robust, high-fidelity flow simulations with low computational cost to attenuate the pressure distortion downstream of the vane. This approach is suitable to any turbomachinery application where strong pressure distortions are dictated by the upstream blade row. In those cases, we could rely on optimizing the single row using high fidelity simulations, without the need of running high computing simulations for the whole stage.

The optimization process is shown to be effective with 43.2% and 56.1% reductions of the pitch-wise static pressure distortion, for the 2D and 3D cases respectively. The parameterization allows to explore widely the design space and offers an original optimized vane passage. The optimal vane 2D section presents a convergent-divergent contraction channel, leading to an over-acceleration of the flow within the channel. The trailing edge shock system is modified and the resulting shock waves that propagate to the following blade row exhibit lower intensity. 3D optimization with lean and section adaption enables further improvements in downstream distortion with no alteration on stage efficiency compared to the baseline.

Subsequently to the vane optimization, the unsteady forcing on the rotor downstream of the optimal vane is computed with a non-linear harmonic method to evaluate the impact on the vane-rotor interaction. Attenuations up to 61% are observed and confirm the reduction in rotor high-cycle fatigue risk. Evolutionary optimization with robust, accurate simulations with low computational cost is therefore shown to reduce the unsteady vane-rotor shock interaction in high-pressure turbines. This result could be used to extend the proposed soft optimization methodology to other applications of rotating machinery encountering shock wave interactions.

4. MULTI-FIDELITY, MULTI-DISCIPLINARY OPTIMIZATION OF COUNTER-ROTATING COMPRESSORS*

This chapter presents the method and the results related to the third objective of the dissertation, i.e. multi-fidelity, multi-disciplinary design optimization of counter-rotating fans.

4.1 Introduction

4.1.1 Counter-rotation in axial transonic compressors

Counterrotating turbomachinery allows reducing the weight of the machine by suppressing the intermediate stator row. Conventionally, rotors in a gas turbine spin in the same direction and stators are used to realign the flow after each compressor or turbine rotor. In a stator-less two-stage counterrotating machine, the two consecutive rotors spin in opposite direction (Figure 4.1), and the second rotor ingests the deviated flow leaving the first rotor. In addition, fast rotational speeds allow reaching high loads and it is common in axial compressors that the tip section travels at supersonic speeds, leading to the emanation of shock waves. Figure 4.2 illustrates a two-dimensional section of a counterrotating compressor, where shock waves (dashed lines) emerge at the leading edge of the profiles (plain lines) due to the fast speed of the wheels. The complex flow features of highly loaded counterrotating compressors make their design a very challenging task. Research on counterrotating axial

*Reprinted with permission from "Multidisciplinary design optimization of a compact highly loaded fan" by Joly, M. M. Verstraete T. and Paniagua G., *Structural and Multidisciplinary Optimization*, Vol. 49, No. 3, 2013, pp. 471–483, DOI: 10.1007/s00158-013-0987-5, Copyright 2013 by Springer, and from "Integrated multifidelity, multidisciplinary evolutionary design optimization of counterrotating compressors" by Joly, M. M. Verstraete T. and Paniagua G., *Integrated Computer-Aided Engineering*, Vol. 21, 2014, pp. 249–261, DOI: 10.3233/ICA-140463, Copyright 2014 by IOS Press.

compressors remains however scarce in the open literature. Studies that achieved designs with low pressure ratio are available [41, 42]. Some experiments of high-pressure ratio counterrotating axial compressors had been performed in the 50s, but limited information about the used geometry was available [43, 44]. More recently, Minato et al. proposed a CFD-based design that achieved a 2.8 pressure ratio [45] and Parker et al. investigated aspirated geometries with a maximum pressure ratio of 3.02 [46] with little information about the design process. Further investigation for a smooth integrated approach is therefore required to enable engineers to design highly loaded, compact counterrotating compressors.

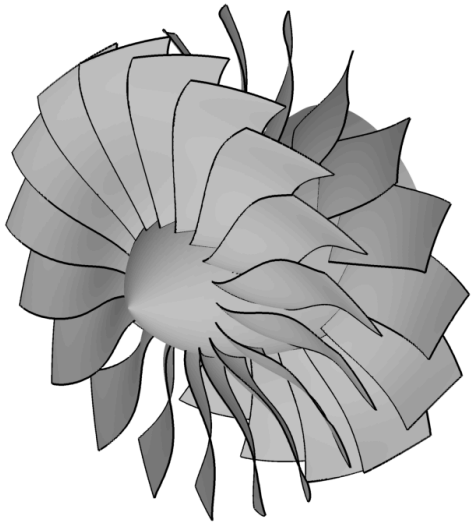

Figure 4.1: Illustration of a counterrotating compressor

4.1.2 Concurrent objectives

The concurrent objectives of high-load and compactness, to reduce weight, require evaluations in terms of aerodynamic performance and structural integrity, which

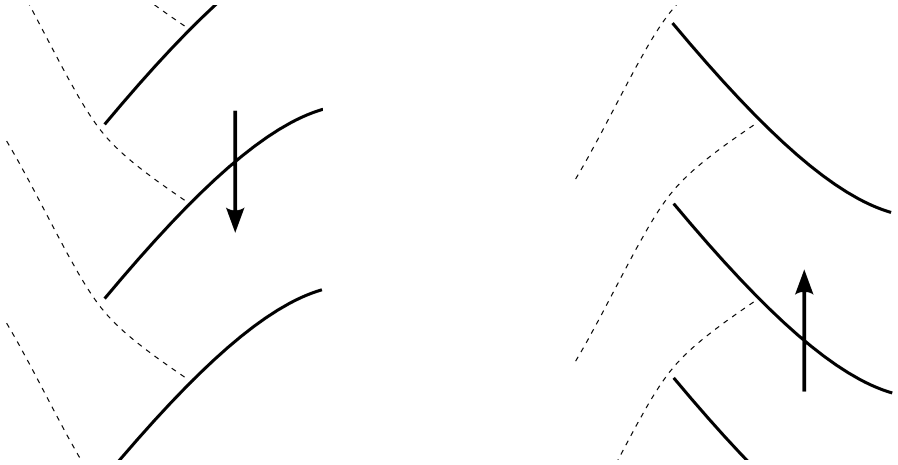

Figure 4.2: Blade-to-blade section of a two-stage transonic counter-rotating compressor with shock waves

adds complexity to the design of axial flow compressors. Several papers have shown the effectiveness of multidisciplinary optimization, considering all involved disciplines simultaneously, to improve the performance of existing configurations [47, 48, 49, 50]. In most studies, the design space includes a large number of parameters, but the range of allowed variations remains meager. The optimized shape improves the performance, but generally with no drastic alterations. The present contribution includes two parts:

In a first part, the multidisciplinary optimization approach is extended to the complete design of a highly loaded compressor. The methodology initiated a new design with no predefined baseline shape. Consequently the design space had to be considerably larger to allow a wide range of possible candidates. The approach comprised two optimization loops (a first for low-fidelity preliminary design and a second for high-fidelity aero-structural design) and led to an innovative design of a single-stage compressor.

In a second part, the first-presented multifidelity approach is extended to facil-

itate the integrated design of counterrotating machines. The lack of empirical and numerical information on the second stage hinders standard design techniques from achieving counterrotation. The key is to use the benefits of evolutionary computing to smooth the handover between the preliminary design and the three-dimensional geometry definition with a novel parameterization based on span-wise distributions. It provides flexible ranges for the design of the detailed geometry within the optimization process, which alleviates the presence of infeasible regions due to unique incidence. Additionally, the method allows the simultaneous design of the two rotors.

4.2 Multi-fidelity, multi-disciplinary approach for single-stage fans

4.2.1 Single-stage compressor design optimization

The traditional strategy the aerodynamic design of transonic compressors consists of four successive steps [51]. A parametric study is first performed with empiric models, such as through-flow solvers, to define a preliminary design. Subsequently, one designs and optimizes several blade-to-blade two-dimensional profiles to generate a three-dimensional geometry. A three-dimensional optimization is ultimately applied to improve the performance, introducing sweep and lean laws to the geometry. A finite element structural analysis is ultimately performed to assess the structural integrity of the geometry. Typically several iterations between inter-disciplinary fields are usually necessary to finalize the design of one rotor.

The main drawback of this traditional method is the parametric study employed during the preliminary design phase. Such an approach is not capable of extensively exploring the whole design space. Secondly, the two-dimensional optimization that generates section profiles does not consider any three-dimensional flow patterns, ignoring for example end-wall effects and secondary flows. The obtained "sub-optimal" profiles then remain constant during the three-dimensional optimization, and the

flow angles prescribed by the empirical model are therefore not improved during the optimization with the high-fidelity solver. Consequently, empirical codes, despite being limited in physical modeling, generally fix 80% to 90% of the final fan design using this traditional method.

The traditional approach is commonly used for the design of transonic fans achieving a pressure ratio of 1.6 (see, for example, [52, 53]). Successful attempts to achieve higher load are however very limited, among which [54] completed a design reaching a 2.1 pressure ratio. Thus, a need exists for more research in the design of highly loaded fans and different approaches have been recently considered. [55] investigated the application of active control by aspiration to enable higher load. [56] suggested a more fundamental analysis to better understand the loss mechanisms induced by high loads.

The current work proposes an enhanced design methodology based on multidisciplinary optimization to achieve the full design of compact highly loaded fans. It aims to smooth the intermediate steps between the preliminary design and the three-dimensional definition of the geometry. The design strategy consists in only two successive steps, a through-flow optimization and a three-dimensional aero-structural optimization. The result is a rapid and smooth design process with a large design space where performances from different disciplines are evaluated simultaneously. This first part targets the design of a compact highly loaded compressor achieving a 2.1 pressure ratio.

The through-flow model is first integrated in an optimization loop to enlarge the design space of the preliminary design. It is crucial to consider a wide range of candidates at this early stage of the design, where the end-walls, the blade count and the wheel speed are selected. Through-flow computations, however, do not include any information about blade geometry; only the solidity (i.e. pitch/chord ratio) is consid-

ered through correlations. It is then proposed to directly initiate a three-dimensional optimization based on the preliminary design results. The parametrization of three-dimensional rotor geometries is based on the stacking along the span of chord-wise camber angle and thickness distributions. Feasible ranges of inlet and outlet metal angles are defined at different radii from possible values of incidence and deviation angles. The second optimization loop evaluates each three-dimensional candidates, simultaneously in terms of aerodynamic and structural performances.

In the results section, two distinct three-dimensional optimizations are performed based on the results of the preliminary design. A first aerodynamic optimization with viscous flow computations evaluates the performance of each geometry candidate in terms of pressure ratio and adiabatic efficiency. The second aero-structural optimization also guarantees the structural integrity of each design candidate with simultaneous fluid and structure evaluations. A finite element solver computes the stress considering centrifugal forcing and flow pressure loading on both suction and pressure sides.

4.2.2 Multi-fidelity approach for compressor design

Because of the complex flow pattern of highly loaded compressor passages (meridional contraction, shock system), the computation of the flow field around a three-dimensional geometry defined by a random set of parameters would likely never converge. An educated guess is required. Based on empirical relations and specified operating conditions, a through-flow solver can provide flow field information upstream and downstream of a blade row along a given meridional flow path.

A through-flow model solves the streamline curvatures and radial gradients at inter-row positions based on the radial equilibrium principle. Losses on the Euler work are introduced based on empirical profile and shock losses. The profile losses

are correlated to the diffusion factor of [57]. Additionally, the normal shock model of [58] is used for transonic sections. The shock-loss coefficient computation is based on the normal shock relations with an upstream Mach number estimated as the inlet relative Mach number expanded by a Prandlt-Meyer angle equal to half of the prescribed relative flow turning on the streamline.

Integrated in an optimization algorithm, the through-flow model is parameterized with the following variables: end-wall heights at hub and shroud up- and downstream (arrows on Fig. 4.3), wheel speed, axial length at hub, and span-wise distribution of solidity (chord/pitch ratio). The inlet total pressure and temperature is specified, as well as targeted values of pressure ratio and mass flow rate. Among the output variables, the following performances could be considered for the objective and constraint functions: mass-averaged pressure ratio, mass-averaged efficiency, mass flow rate and number of blades. Span-wise distribution of diffusion factor, loss coefficient, inlet and outlet flow angles as well as velocities, Mach number, pressure and temperature are also available. A through-flow model provides information about the flow upstream and downstream of the blade row. No information about the blade geometry is provided; only solidity, end-wall contours and blade count are known at this stage.

The approach to generate and modify the design candidates is determined by the parametrization. Hence, the parameterization is a crucial step in the definition of the optimization problem. In the present study, compressor blade profiles are defined by a thickness distribution along a camberline. The stacking of several profiles along the span leads to a three-dimensional geometry.

The camber turns the flow from an inlet flow angle to an outlet flow angle. The first and last angles of the camberline are called inlet and outlet metal angles. The difference between the flow angle and the metal angle are called incidence and

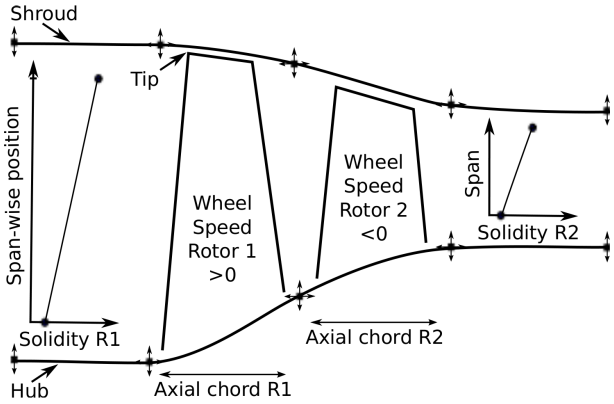

Figure 4.3: Flow path parameterization

deviation, for the inlet and the outlet respectively.

To initiate the compressor blade design, the flow angles values prescribed by the through-flow solver are used as a guess of blade metal angles (or beta-angle). Incidence and deviation tables [59] are then used to set the range of feasible inlet and outlet blade metal angles at different span-wise locations. A camberline is generated with B-Spline parametric curves. In addition to the value of inlet and outlet metal angles, intermediate angle points can be defined to form a set of control points of a camber-angle distribution. This distribution is then integrated to generate the camberline (See Fig. 4.4, top left).

A three-dimensional cambersurface is created from the stacking of several camberlines at different radii (See Fig. 4.4, left). Span-wise distributions of lean and sweep are introduced to define the stacking of the camber lines. Sweep is an offset applied along the stagger line (line from leading edge to trailing edge), while lean defines the offset perpendicular to the stagger line. (See Fig. 4.4, bottom).

Thickness complements the blade definition. At several span-wise positions, dif-

ferent thickness distributions are defined with B-Spline curves and applied symmetrically to the cambersurface (See Fig. 2, center right). The two first control points are dependent to guarantee a G2 continuous leading edge. At each span-wise positions, blade contours include a suction and a pressure side. A loft of the several contours leads to the generation of a suction and a pressure three-dimensional B-Spline surfaces, which characterize the blade geometry.

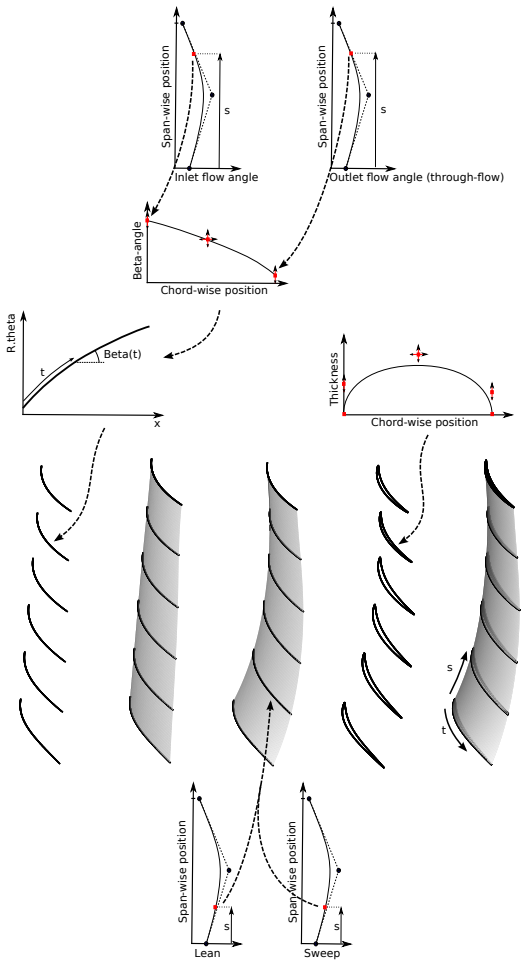

Figure 4.4: Parametrization of three-dimensional geometry

4.2.3 Multi-disciplinary high-fidelity performance evaluation

To achieve the full design of a compressor, different levels of fidelity are used to evaluate the performance. Empirical relations are employed in the preliminary design. Then, accurate computational solvers enables one to evaluate the performance of a parametrized blade geometry. A Computational Fluid Dynamics (CFD) solver computes the blade aerodynamic performance, while a Computational Structural Mechanics (CSM) solver is used to guarantee the structural integrity of the geometry.

4.2.3.1 Aerodynamic performance evaluation

The fluid domain is defined within the B-spline surfaces of the suction and pressure sides of two adjacent blades and the circumferential end-walls. The domain is discretized using a finite volume grid. First, a two-dimensional grid in the meridional plane is generated with a clustering near the walls. The tip clearance is defined as 1% of the blade height at the leading edge. For each stream-wise grid line in the meridional plane, a surface of revolution is constructed, and the intersection with the blade is computed. A structured grid in this surface is generated using an elliptic smoother. The single-block blade-to-blade mesh has a non-matching periodic boundary, which enables limiting the skewness of the grids in the throat region of the highly cambered tip sections (See Fig. 4.5). The collection of all stream-wise blade-to-blade grids are stacked along the radial direction to construct the structured single-block that defines the full three-dimensional grid being shown in Figure 4.6. This grid generation procedure is parameterized to enable its automatic execution within the optimization.

The three-dimensional viscous-flow solver TRAF 3D [37] is used to evaluate the fluid performance of compressor geometries. The Reynolds-averaged Navier-Stokes

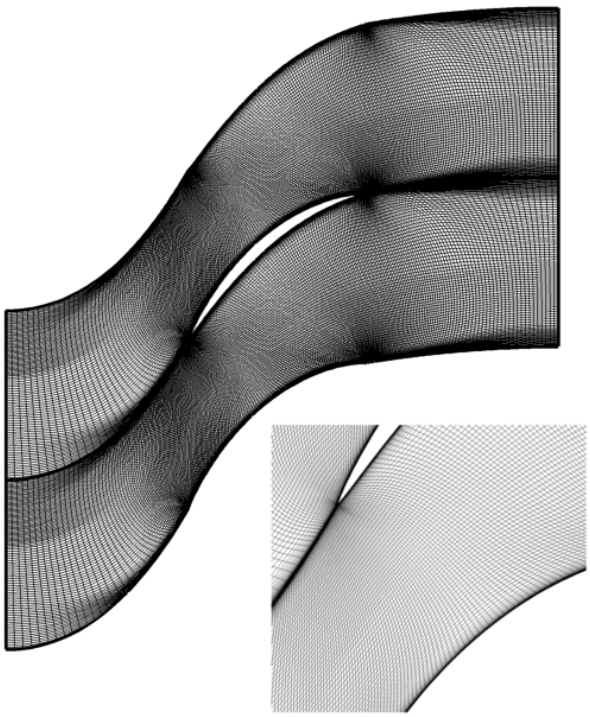

Figure 4.5: Blade-to-blade H-type mesh with quality cells in the throat region

equations are solved using a Runge-Kutta scheme. A low level of artificial dissipation is guaranteed by eigenvalue scaling. The two-layer eddy-viscosity model of Baldwin and Lomax is used for the turbulence closure. The acceleration strategies of variable-coefficient implicit residual smoothing and full-approximation-storage multigrid scheme of Brandt and Jameson are implemented. TRAF 3D has been previously validated using the NASA rotor 67 transonic fan [37]. A similar grid size to the one used in this validation test case is employed in the present work.

4.2.3.2 Structural performance evaluation

Flow pressure loads have to be considered, in addition to centrifugal forces, to assess the static mechanical response of a spinning blade row. The unsteady fluid-

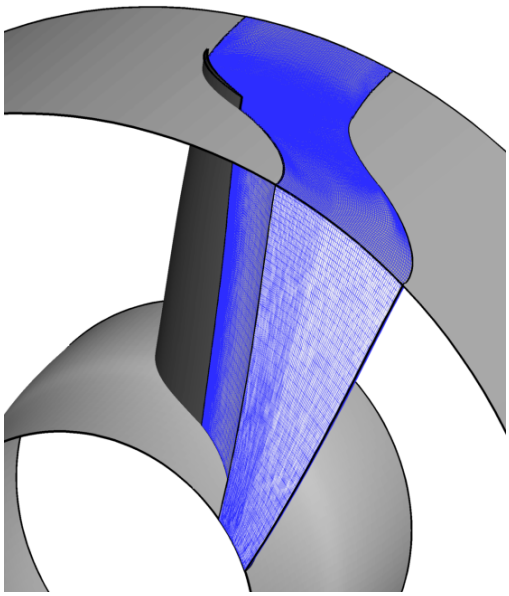

Figure 4.6: Fluid mesh around blade and end-walls

structure interaction are not considered here, because their integration in optimization problems remains computationally intractable with modern computers.

Subsequently to the fluid domain generation, which comprises the suction and pressure sides, the blade geometry is complemented with a root. A fillet radius is introduced and defined as 3% of the blade height at the leading edge. The Delaunay triangulation method is then applied to generated a three-dimensional finite element grid (See Figure 4.7).

The solver Calculix [60] is used to compute the von Mises stresses in the blade, based on the properties of titanium (See Table 4.1). The following boundary conditions are applied:

- Centrifugal force
- Flow pressure load on both sides of the blade
- Constraints on the root faces

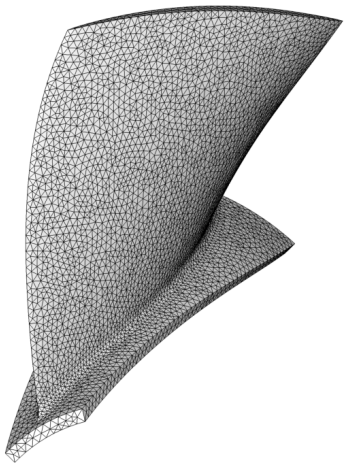

Figure 4.7: Detailed view of the hub fillet radius

Density (g/cm^3)	4.5
Young's modulus (GPa)	116
Poisson ratio	0.32
Yield strength (MPa)	940

Table 4.1: Mechanical properties of titanium

Flow pressure values from the fluid solution are considered during the structure analysis. At each FEM node on both suction and pressure sides, the flow pressure value is interpolated from the fluid evaluation results with an inverse distance-weighted method [61]. The interpolation is therefore influenced most by the nearby points and less by the more distant points. The FEM elements sharing a face on the blade sides are retrieved, and a pressure value is assigned to the face on the side, computed as the average of the values on its three corners. Figure 4.8 shows the pressure field on the suction side as a CFD result (left) and after interpolation on the FEM grid (right).

The constraints on the root could be of two different natures. Either the root

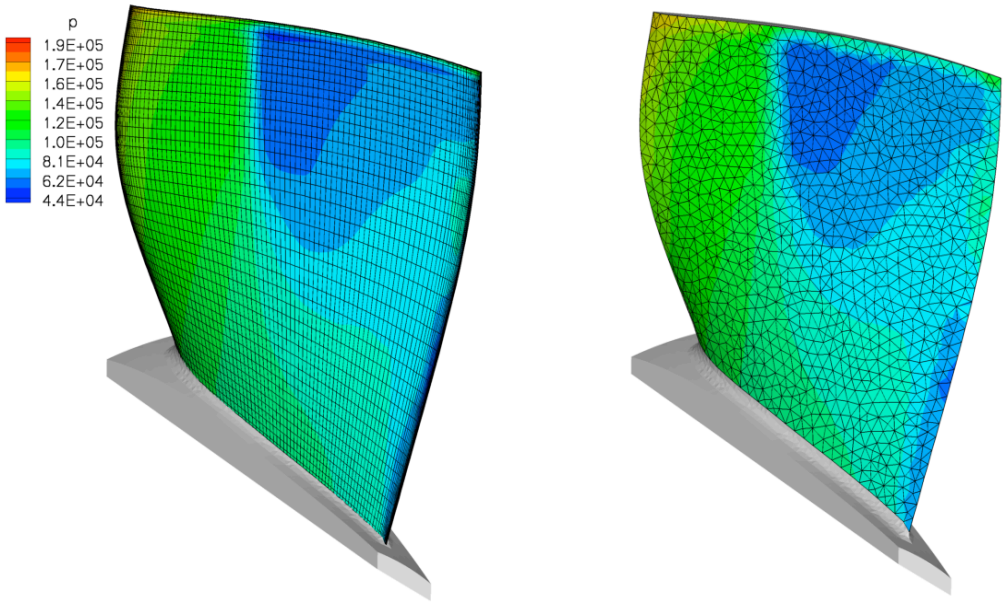

Figure 4.8: Flow pressure values on suction side of CFD mesh (left) and FEM mesh (right)

slides into a groove and fixed translational degrees of freedom are imposed on the five faces in contact with the groove. Alternatively, one could consider the roots of two adjacent blade in direct contact and symmetric boundary conditions are imposed.

The authors consider the blade under operating conditions. Due to the high stiffness of the blade, the displacements in transonic fans are small [62], which guarantees that the stress computations on the deflected blade are sufficiently representative of the stress that one would find on the undeflected blade (unknown at this stage). Therefore it is adequate to consider a single CFD computation followed by a single FEM computation, using the aerodynamic pressure fields on the sides of the blade as loading. Once the blade is optimized, the displacements are subtracted from the geometry to determine the actual shape to be manufactured.

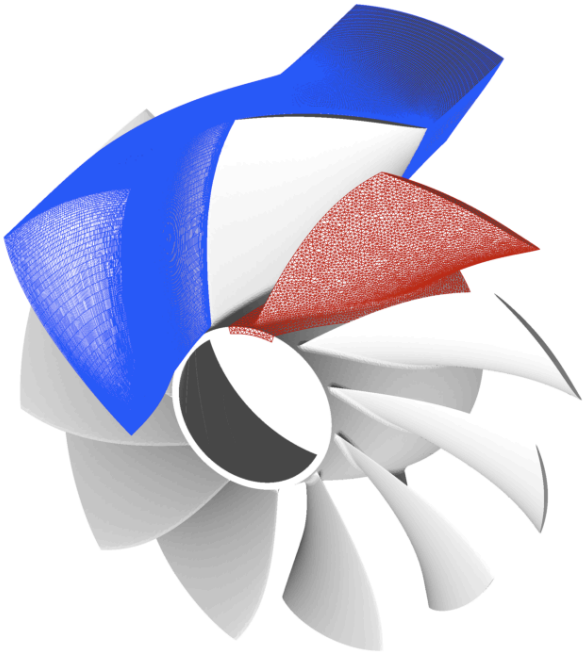

Figure 4.9: CFD and CSM grids on a compressor blade row

4.2.4 Results

The methodology was applied to design a highly loaded compressor achieving a 2.1 pressure ratio. It had to provide a mass flow rate of 20.2 kg/s at atmospheric conditions. The design strategy consisted in two successive steps, a through-flow optimization and a three-dimensional aero-structural optimization.

4.2.4.1 Through-flow optimization

The objectives of the through-flow optimization, written in their minimization form, were:

- *1-η*: Maximize the predicted efficiency
- *Tip radius*: Minimize the machine size, considering the end-wall tip radius parameter as a objective

- *for* $M_{1ri} > 1.0$, *max*$(\beta_{2i} - \beta_{1i})$: Minimize the highest value of relative flow turning over the spans of supercritical profiles, limiting the risk of boundary layer separation at the shock impingement on the adjacent blade suction side

The obtained pressure ratio was constrained to the range [2.1; 2.2]:

- $2.1 <$ Po2/Po1 < 2.2

The design space, i.e. list of parameters with their range, is summarized in Table 4.2.

Parameter	Lower limit	Upper limit
Wall height at shroud upstream (cm)	10	40
Passage height upstream (cm)	5	30
Wall height reduction at shroud (cm)	0	5
Wall height increase at hub	0	15
Wheel tip speed (m/s)	200	450
Axial length at hub (cm)	5	15
Solidity at hub	1.4	1.5
Solidity at tip	2.0	2.2

Table 4.2: Design space for through-flow optimization

Figure 4.10 shows Pareto fronts as a result of the through-flow optimization with 200 generations with 100 individuals in each population. It can be observed that a higher tip radius allows a higher efficiency and a limited relative flow turning over the span of supercritical profiles. Nonetheless, our interest remains in a reduced radius to achieve maximum compactness, which guided the authors to select one optimum among the candidates of the Pareto front.

The selected candidate, denoted by a diamond in Figure 4.10, is summarized in Table 4.3. The configuration obtained was a transonic fan with a subsonic inlet

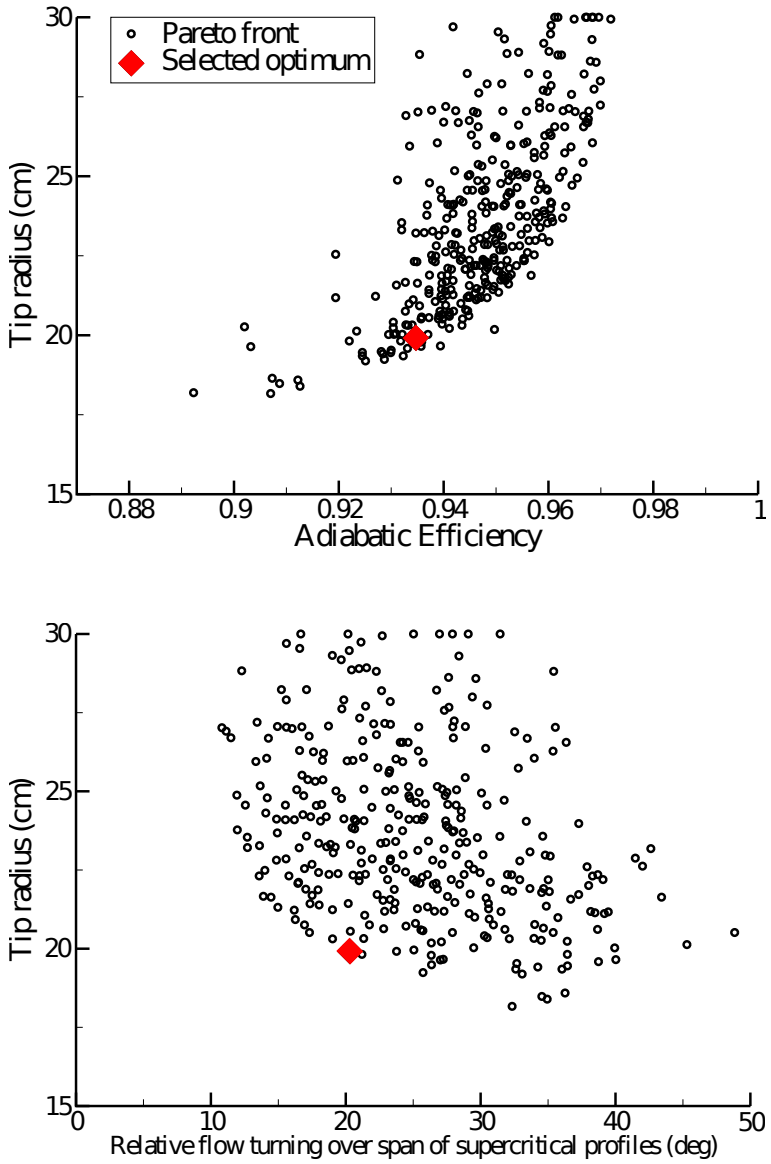

Figure 4.10: Pareto fronts of through-flow optimization (tip radius vs adiabatic efficiency on top, tip radius vs relative flow turning over supercritical profiles on bottom)

relative Mach number of 0.58 at the hub and a supersonic value of 1.42 at the tip. The maximum relative flow turning over the spans of supercritical profiles is about 20 deg.

Po2/Po1	2.14
Wheel speed (RPM)	21711
Tip Radius (m)	0.199
Tip Speed (m/s)	442
Blade count	14
Mass flow (kg/s)	20.2
M1r hub	0.58
M1r tip	1.42
Solidity hub	1.41
Solidity tip	2.05

Table 4.3: Optimum after through-flow optimization

4.2.4.2 Aerodynamic optimization

The three-dimensional optimization was constrained to produce fan geometries achieving a pressure ratio between 2.1 and 2.2 with a minimum required mass flow rate of 20.2 kg/s at the design point:

- $2.1 < \text{Po2/Po1} < 2.2$
- $\dot{m} > 20.2$

The objective was to maximize the design-point adiabatic efficiency. The list of parameters with their range, is summarized in Table 4.4.

After 60 populations of 40 individuals, the optimal fan geometry provided a pressure ratio of 2.11 with an efficiency of 89.1%. In Figure 4.11, the performance maps

Parameter	Lower	Upper
Inlet metal angle at hub (deg)	30	50
Inlet metal angle at 50%-span (deg)	40	60
Inlet metal angle at tip (deg)	50	70
Intermediate camber change at hub (deg)	10	30
Interm. camber change at 50%-span (deg)	0	20
Intermediate camber change at tip (deg)	0	20
Outlet camber change at hub (deg)	10	30
Outlet camber change at 50%-span (deg)	0	20
Outlet camber change at tip (deg)	0	20
Position of interm. camb. at hub (% chord)	0.2	0.8
Position of interm. camb. at 50%-span (% c.)	0.2	0.8
Position of interm. camb. at tip (% c.)	0.2	0.8
Intermediate thickness at hub (% c.)	0.005	0.01
Intermediate thickness at 50%-span (% c.)	0.004	0.01
Intermediate thickness at tip (% c.)	0.0035	0.01
Position of interm. thick. at hub (% c.)	0.2	0.8
Position of interm. thick. at 50%-span (% c.)	0.2	0.8
Position of interm. thick. at tip (% c.)	0.2	0.8
Lean at 50%-span (% c.)	-0.1	0.1
Lean at tip (% c.)	-0.1	0.1
Sweep at 50%-span (% c.)	-0.1	0.1
Sweep at tip (% c.)	-0.1	0.1

Table 4.4: Design space for aerodynamic optimization

are complemented with an indication (dashed lines) of the first observed instabilities seen in the Navier-Stokes convergence as the machine was throttled.

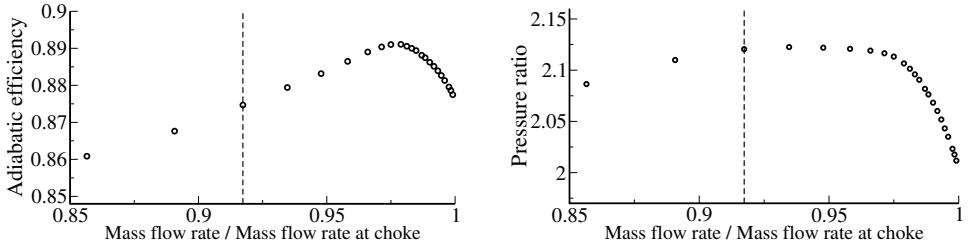

Figure 4.11: Optimal fan geometry performance (efficiency curve on left, pressure ratio on right)

Figure 4.12 shows how the optimal geometry achieved compares to the results of the through-flow model. The latter prescribed distributions of relative flow angles with higher turning at the lower spans, as a result of the objective to limit flow turning in supercritical profiles during the first optimization cycle. After the fluid optimization, a large amount of the relative flow turning moved towards the higher spans. The load distribution also presents a steeper distribution, which tends to indicate a higher contribution of the shock to the compression. The efficiency shows a net drop above 80% of the span, which is expected as tip clearance losses were not predicted by the through-flow model. The density field on the suction side (See Fig. 4.13) confirms the transonic configuration of the fan, as the impingement of the passage shock on the surface is observed only on the top half of the span.

The behavior of the computed fan flow was compared to theoretical investigations of profiles subject to a supersonic inlet Mach number [63]. In transonic fans, a shock system impinges the suction side at higher spans. The high rotational speed of the blade makes the section profiles at high radius reach supersonic speeds. Consequently,

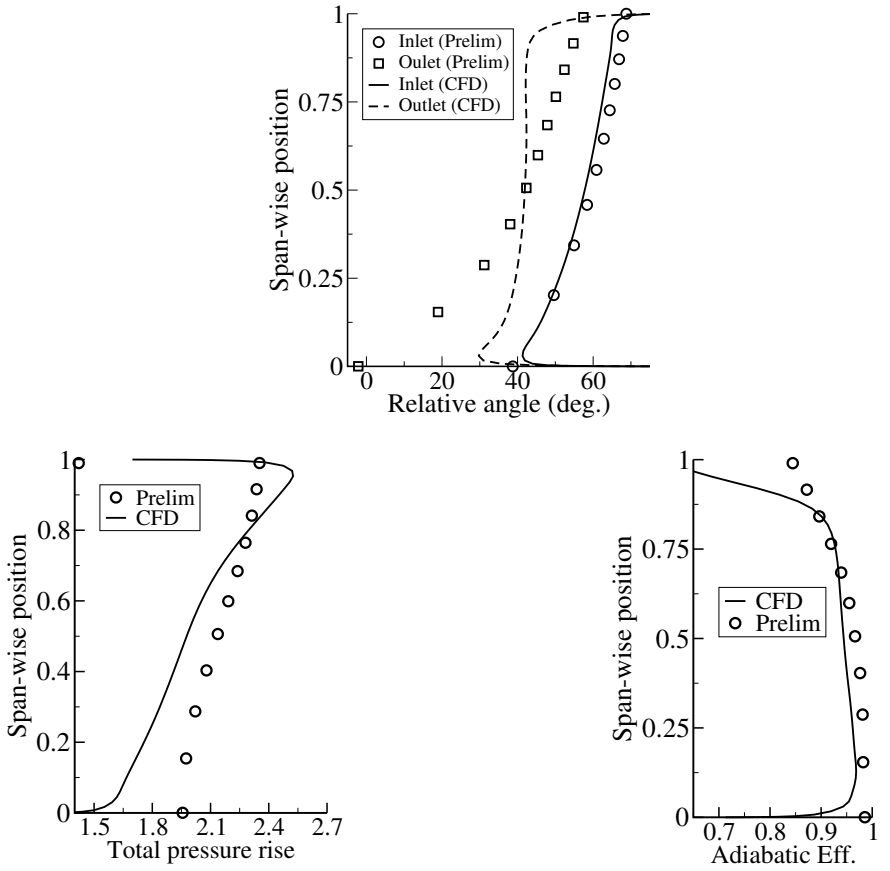

Figure 4.12: Distributions of relative flow angles (top), total pressure rise (bottom left) and adiabatic efficiency (bottom right) compared after through-flow and CFD optimizations

a shock originates at the leading edge, with a right-running part hitting the suction side of the adjacent blade and a left-running part propagating upstream.

In Figure 4.14, dashed lines indicate the direction of the periodic left-running shocks. The inlet flow travels across the successive oblique shocks, remaining supersonic up to the front suction side. Expansion waves emanate from the convex surfaces and accelerate the surrounding flow. The Mach number level increases to reach its highest values just upstream of the right-running shock. This strong normal shock impacts on the suction side of the adjacent airfoil, and decelerates abruptly the su-

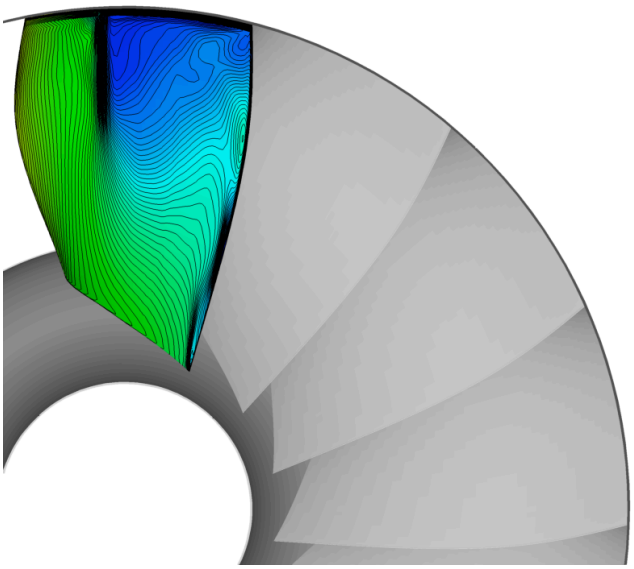

Figure 4.13: Fan geometry with density field on the suction side

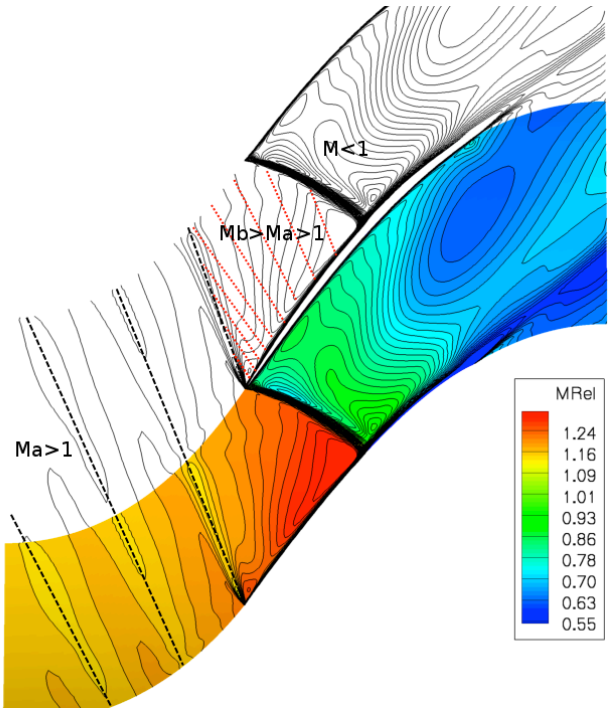

Figure 4.14: Density field and Mach number levels at design point, 80% of span

personic flow into the subsonic regime. The higher the flow turning in the supersonic part, the stronger the right-running shock. To limit the boundary-layer/shock interactions, the optimum configuration happens to provide most of the turning in the subsonic region. The flow in the region close to the front suction side is supersonic, and its inclination is therefore influenced by the shape of the suction side surface. The Mach number upstream of the profile and the inlet flow angle are not independent of each other. There is one particular incidence, the unique incidence [63], at which operation is possible.

Considering off-design operations, this shock system at the higher spans changes as the machine is throttled. At the choke point (lower back pressure and higher mass flow rate than design point, see Fig. 4.15, left), a double shock system occurs in the throat with a weak shock attached to the leading edge followed by a strong passage shock. At the design point (See Fig. 4.14), the oblique shock and the passage shock merge into a single shock. This is the optimal loss configuration. As the back pressure increases, the shock system moves ahead of the leading edge, eventually leading to stall (See Fig. 4.15, right).

4.2.4.3 Aero-mechanical optimization

The von Mises stress evaluation reveals that the aero-optimal geometry exceeds the titanium yield strength limit with a maximum value of 1972 MPa (See Figure 4.16). The stresses are distributed along the whole chord and span of the geometry. Stress peaks are understood to originate from strong camber change along the span. Figure 4.17 (left) illustrates a superposition of hub and tip section profiles projected on the circumferential plane. Even though very little contribution of lean and sweep is observed, severe span-wise evolution of the leading- and trailing-edge position are shown by the curve linking the two profiles. Also, important stresses

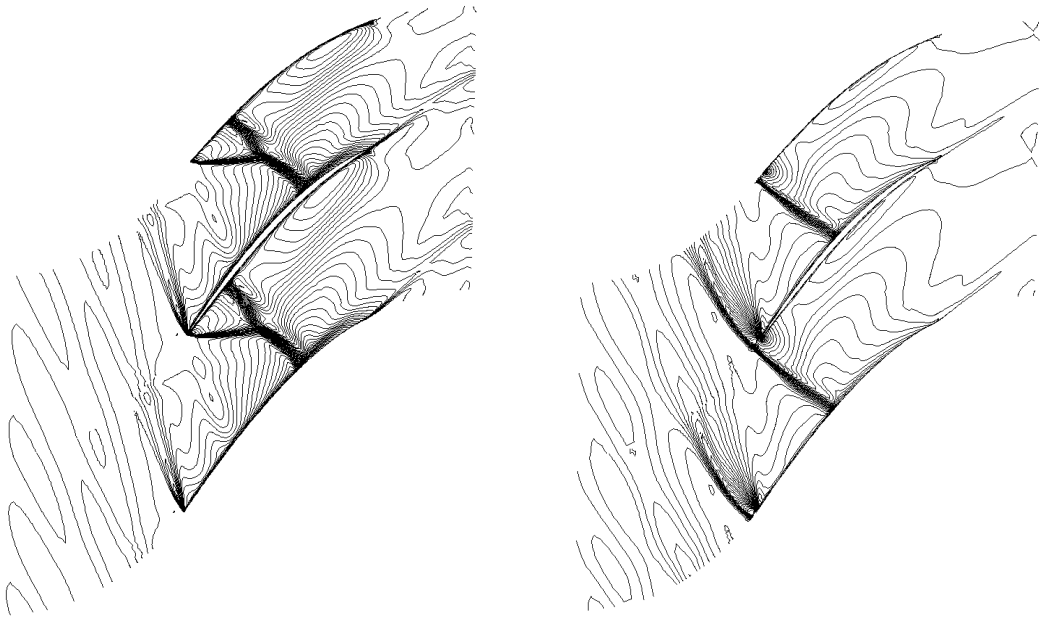

Figure 4.15: Density field at choke point (left) and near the stall point(right), 80% of span

are located at the hub on the pressure side where material extension occurs as the blade bends towards the suction side (See Figure 4.16) due to the centrifugal force and flow pressure loading.

A multi-disciplinary optimization was then performed aiming to reduce the maximum von Mises stress while increasing the flow efficiency. The optimization shared the same parametrization and constraints as the previous aero-only design case. The authors choose to consider the stress as an objective in the present work to find trade-offs between stress and performance, so to allow a better judgment regarding impact of safety on efficiency.

The objectives are:

- Adiabatic efficiency
- von Mises stress

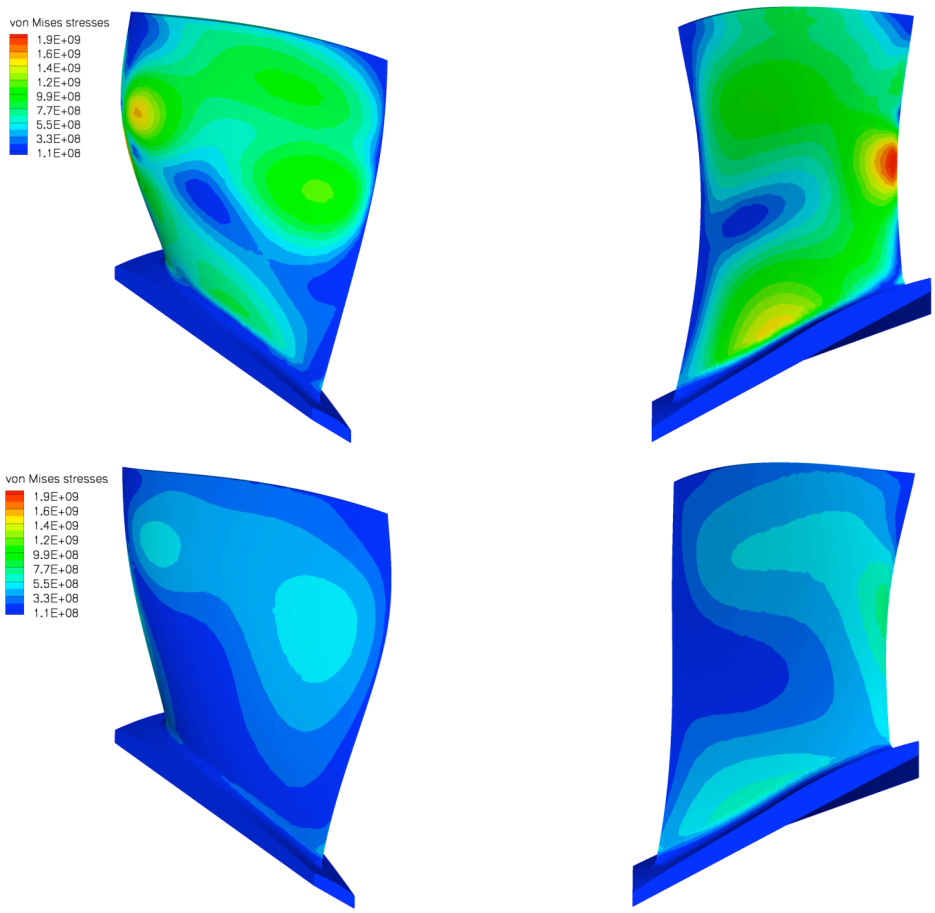

Figure 4.16: von Mises stress distribution on suction side (top left) and pressure side (top right) of aero-optimal fan geometry and on suction side (bettom left) and pressure (bottom right) of finalized fan geometry

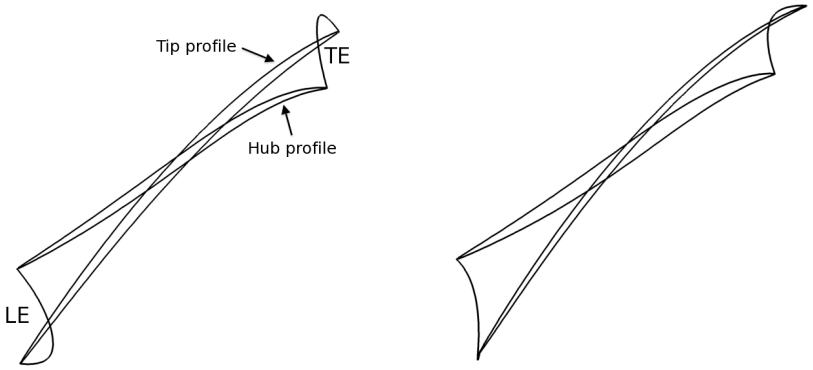

Figure 4.17: Section profiles with leading- and trailing-edge spanwise position for the aero-optimal (left) and finalized (right) designs

And the constraints are:

- $2.1 < \text{Po2/Po1} < 2.2$
- $\dot{m} > 20.2$

After 20 populations of 40 individuals a geometry was selected. It provided an efficiency of 88.4% with similar flow features to the previous design. Figure 4.18 shows that a small amount of relative flow turning and pressure rise decreased along the span. Structurally, the new design achieved a reasonable safety margin with a maximum von Mises stress of 639 MPa, which represents a 65% reduction compared to the aero-optimal design. The stress intensity on the blade was strongly reduced, as shown in Figure 4.16. This attenuation is understood as an effect of the smoother span-wise change of camber and a larger profile thickness at the hub (See Figure 4.17).More generations would very likely lead to further enhanced performance, which let the authors think that the prospects of the proposed methodology are promising.

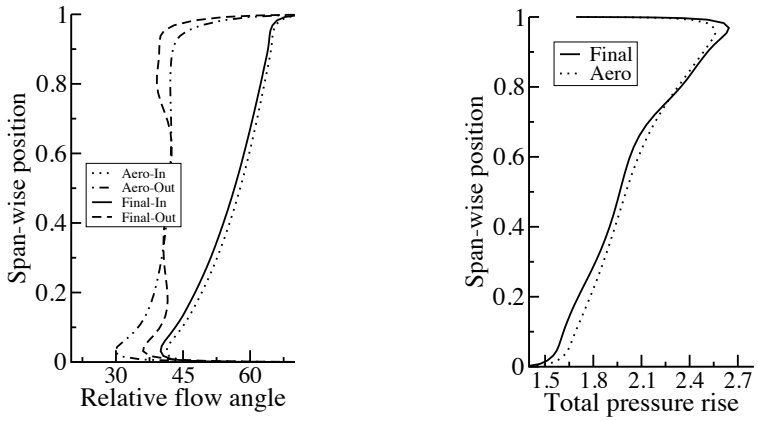

Figure 4.18: Span-wise distributions of relative flow turning (left) and total pressure rise (right) for aero-optimal and finalized fan geometries

4.3 Multi-fidelity, multi-disciplinary approach for counter-rotating fans

4.3.1 Counter-rotating compressor design optimization

The above presented multi-fidelity, multi-disciplinary approach is extended to facilitate the integrated design of counterrotating machines. The lack of empirical and numerical information on the second stage hinders standard design techniques from achieving counterrotation. The key is to use the benefits of evolutionary computing to smooth the handover between the preliminary design and the three-dimensional geometry definition with a novel parameterization based on span-wise distributions. The use of a limited physical model and, subsequently, of a high-fidelity solver has a considerable impact on the design of complex turbomachinery. Without such an approach, a traditional optimization method would suffer to a large extent finding a good solution. The design optimization of three-dimensional compressor blades demonstrates an extended level of infeasible regions, because supersonic flow phenomena (i.e. the shock system mentioned above) can prevent the flow solver to converge. It is well known that a high level of infeasible designs, where no valid solution for the objectives and constraints can be obtained, leads to a very complicated optimization process, regardless the choice of optimization method. Tests performed by the authors, where no advantage of the multi-fidelity approach was used, demonstrated indeed that no solution could be found using a standard optimization approach, because the entire first generation consisted of non-converged individuals. This paper shows that problems with a large amount of infeasible designs can still be effectively solved with a two-level evolutionary approach. The first level with reduced physics and lower computational cost helps the optimization process to avoid infeasible regions for the flow solver within the large design space. The method incorporates eventually increasing levels of fidelity, with a second level based on high-

fidelity solvers. This multi-fidelity, multi-disciplinary integration is made possible by the use of an evolutionary algorithm. Applied to counterrotating machines, the convenient handover between the preliminary design and the three-dimensional geometry definition allows accounting for the lack of empirical and numerical information on the second stage. It provides flexible ranges for the design of the detailed geometry within the optimization process, which alleviates the presence of infeasible regions due to unique incidence [64, 65]. Additionally, the method allows the simultaneous design of the two rotors.

4.3.2 Parameterization for counter-rotating blades

The outputs of the preliminary flow path design are, for each rotor, end-wall heights at the hub and the shroud, axial chords at the hub, and span-wise distributions of solidity. In addition, the model estimates inter-row flow properties, including the relative flow angles. This information is also used to initiate the three-dimensional design optimization of the rotors.

Differently from conventional design approaches where camberlines are generated at discrete specific radial positions, a new parameterization based on span-wise distributions is developed within the current work to relate conveniently with the information predicted by the empirical model. Camberlines are defined as continuously varying functions along the span-wise direction. This allows first having inlet and outlet metal angles distributions defined exactly within the flow path, providing a direct link to results from the flow path design. It also ensures a smooth evolution along the span, preventing from sharp variations that are both aerodynamically and mechanically undesirable [64].

Figure 4.19 illustrates the rotor geometry generation process of the novel parameterization. Several BSpline parametric curves define five distinct span- wise

distributions. Four are used to define the span-wise variation of metal angles, including the inlet and outlet angles as well as an intermediate angle with variable position along the chord. The last distribution defines the axial chord along the span.

Extracting the values at a specific span-wise position (s, as shown on Figure 4.19, A), one generates a metal angle distribution along the chord by defining the control points of a second order Bezier curve. By integration, a camber profile along the axial chord is built in the (x,Rθ) plane. Then, one interpolates the end-wall curves to build a meridional streamline at a constant span-wise position (see B in Figure 4.19). Based on the axial length extracted at this span-wise position, this line is axially centered. Combining the camber profile and the meridional streamline, one creates a three-dimensional camberline. This process is repeated for several span-wise positions and eventually leads to generate a three-dimensional camber surface.

Two additional span-wise distributions of lean and sweep are introduced and affect the stacking of the different camberlines. Sweep is an offset applied along the stagger line (the line joining the leading and trailing edges), whereas lean describes how the camberlines are stacked along the direction normal to the stagger line [64]. The thickness distributions complement the blade definition. At several span-wise positions, BSpline curves define thickness distributions that are applied symmetrically to the camber surface [50]. The blade contours include suction and pressure sides.

4.3.3 Results

The methodology is applied to the design of a two-stage vane-less counterrotating compressor. The target is to achieve high pressure, high efficiency and compactness. First, the flow path is defined by optimization with a low-fidelity model. Then, the

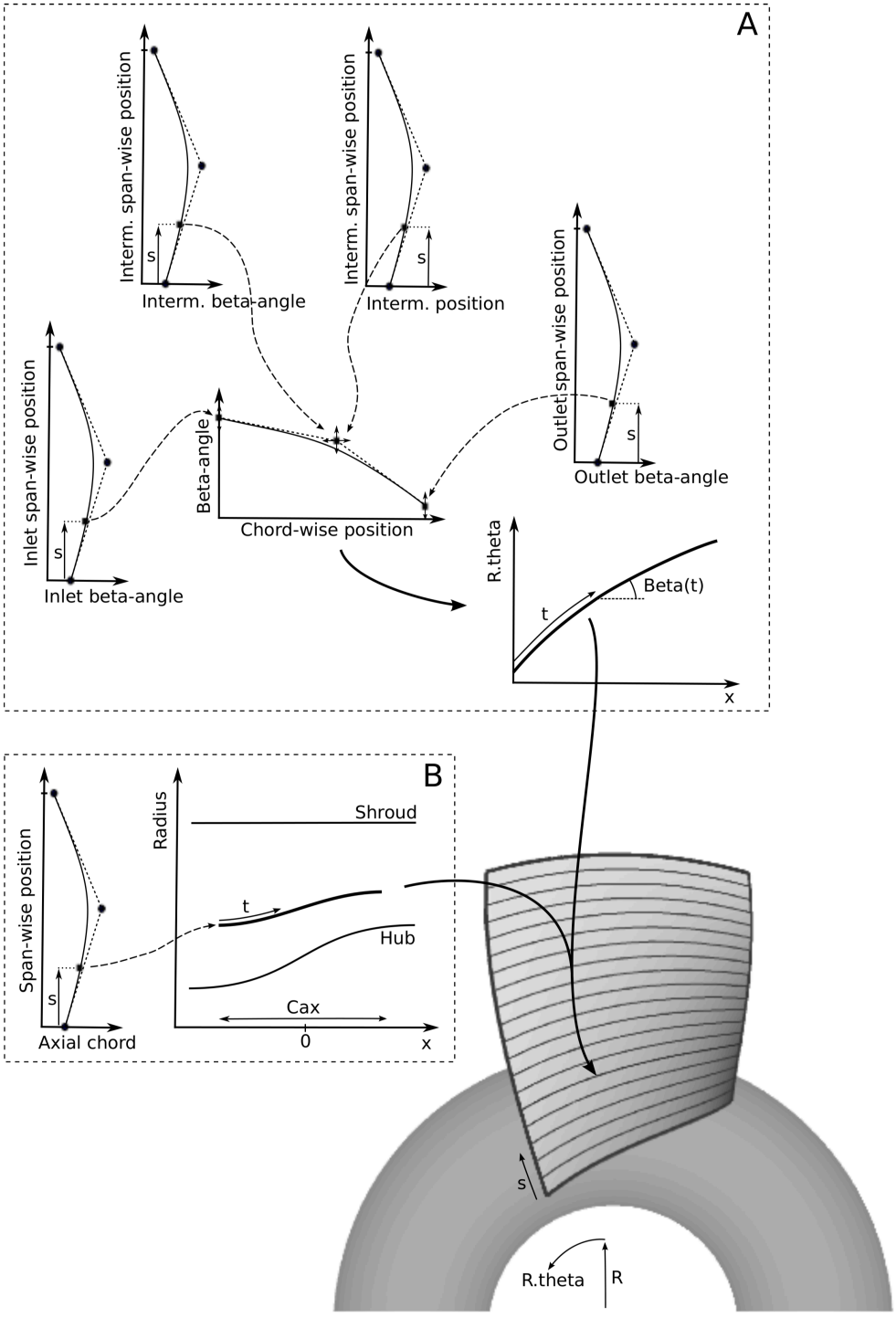

Figure 4.19: Rotor cambersurface parametrization

detailed design of both rotors is performed with the aero-structural optimization of three-dimensional blade geometries.

4.3.3.1 Flow path design optimization

The machine has to provide a 20.2kg/s mass flow rate at the standard conditions (pressure of 101325Pa and temperature of 293K). The objectives are:

- Maximize overall pressure ratio for high load
  Po1, Po3: inlet, outlet total pressure
- Minimize loss coefficient, , for efficiency
- Minimize tip radius, rTip, for compactness

Although defined as an objective, the accumulated pressure ratio is also constrained to be superior than 2.1 to exclude design candidates achieving too low pressure ratios. The maximum flow turning on streamlines with relative supersonic inlet is con-strained to be below 30 degrees. The constraints are:

- Constrain overall pressure ratio
- Limit the relative flow turning to 30 degrees over the span of supercritical profiles (i.e. inlet relative Mach number, M1ri, above unity)

The design space is summarized in Table 4.5. Based on the previously successful transonic single-row compressors [54], solidities of about 1.5 and 2.0 seem to operate efficiently for inlet relative Mach number of 0.8 and 1.5, respectively. The solidity ranges for the current counterrotating design are chosen based on the expectation of a transonic first stage (inlet relative Mach number range from subsonic at the hub to supersonic at the tip) and a supersonic second stage (supersonic inlet relative Mach

number along the whole span). In the present study, the axial spacing in-between the two rotors is fixed.

Parameter	Lower limit	Upper limit
Wheel tip speed rotor1 (m/s)	-450	-200
Wheel tip speed rotor2 (m/s)	200	450
Tip height inlet (cm)	10	40
Tip height decrease at inter-stage (cm)	0	5
Tip height decrease at outlet(cm)	0	5
Hub-shroud height difference at inlet (cm)	5	30
Hub height decrease at inter-stage (cm)	0	15
Hub height decrease at outlet(cm)	0	15
Axial chord for both rotor (cm)	5	15
Solidity rotor1 at tip	1.9	2.1
Solidity rotor1 at hub	1.4	2.1
Solidity rotor2 at tip	1.9	2.1
Solidity rotor2 at hub	1.9	2.1

Table 4.5: Design space for low-fidelity optimization

Figure 4.20 illustrates the objective space with the Pareto fronts available after 500 generations of 100 individuals. With each evaluation taking about 3 seconds of CPU time, the whole optimization time consumes about 2 days on a single core. A clear Pareto front is visible with both projected plots and highlights the conflicts between the three objectives.

The optimum candidate is selected to achieve a pressure ratio of about 3.0 with the minimal possible losses and acceptable size (the authors gave more priority to the two objectives of high load and efficiency than to the one of compactness). It is illustrated as a large circle in Figure 5 and its characteristics are summarized in Table 4.6. The selected flow path shows a prediction of inlet relative Mach number

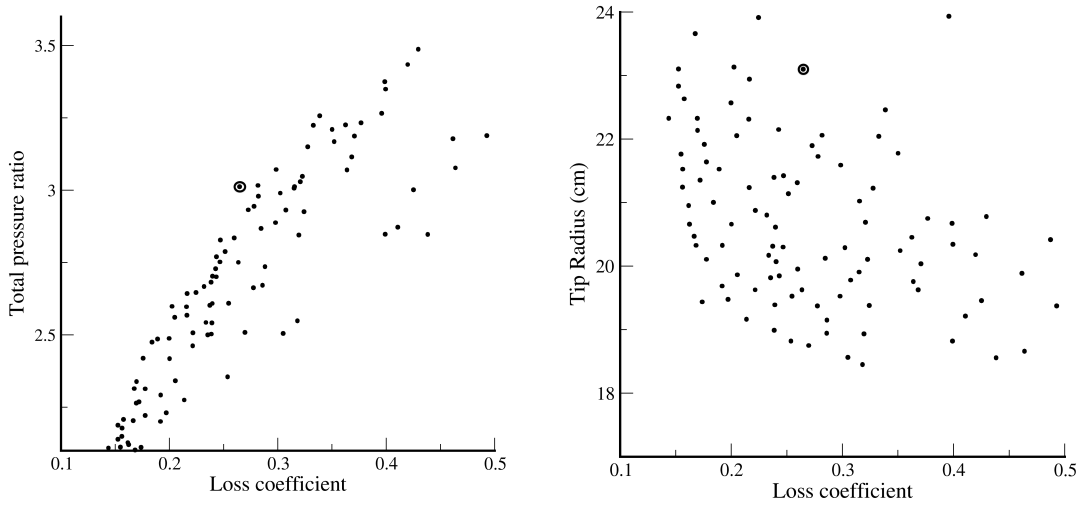

Figure 4.20: Projections of the three-dimensional Pareto front for low-fidelity optimization

Accumulated pressure ratio	3.012
Accumulated efficiency	0.816
Tip radius (cm) at inlet	23.10
Tip radius (cm) at inter-stage	23.10
Tip radius (cm) at outlet	21.93
Hub radius (cm) at inlet	11.74
Hub radius (cm) at inter-stage	16.50
Hub radius (cm) at outlet	17.67
Pressure ratios for both rotors	1.94/ 1.55
Adiabatic efficiency for both rotors	0.898/ 0.742
Tip speed for both rotors (m/s)	-443.1 / 295.5
Wheel speed (RPM)	-18316.5 / 12217.5
Blade count for both rotors	27 / 30
Inlet relative Mach number at hub	0.785 / 1.295
Inlet relative Mach number at tip	1.410/ 1.359
Solidity at hub for both rotors	1.80 / 2.09
Solidity at tip for both rotors	1.93 / 1.91

Table 4.6: Optimum flow path after low-fidelity optimization

at the tip of 1.41 and 1.36 for the first and second rotor, respectively. These values remain in a suitable range for the design of efficient transonic compressor profiles [66]. The predicted relative flow angles distributions are used to initiate the sub-sequent rotor three-dimensional geometry optimization.

4.3.3.2 Rotor design optimization

The high-fidelity optimization defines the detailed design of both rotors considering CFD and CSM performances. The design space includes a total of 60 parameters, 30 per rotor, listed in Table 4.7. Each span-wise distribution of metal angles or axial chord is defined by three control points (hub, 50% span, tip). From the flow angles distributions prescribed by the low-fidelity solver, ranges of possible metal angles, i.e. camberline angles, are chosen considering incidence and deviation. In turbomachinery, incidence and deviation are the angle differences between the flow angles and metal angles at the inlet and outlet of the blade profile respectively. The adopted strategy is that the low-fidelity model has identified an optimal flow path. This flow path might however not be optimal in the more detailed CFD analysis used in the three-dimensional process. Moreover, to translate the through-flow results to blade angles, one needs incidence and deviation distributions, which depend on the profile shape. To account for these unknowns, a range to the blade angles is set in the three-dimensional optimization and allows altering the low fidelity prescriptions and identifying at the same time optimal incidence angles. The deviation is also implicitly accounted for in the present strategy. For the intermediate control points, described in Figure 4.19, A, the blade metal angle and its axial position are al-lowed to change within two relative limits: 20 to 80% of the inlet and outlet angles and of the chord length respectively. The mass flow rate is constrained to be superior to 20.2 kg/s and the maximum von Mises on both rotors is imposed to offer a safety

Parameter	Lower	Upper
Rotor1 Inlet Metal Hub (deg)	-65	-45
Rotor1 Inlet Metal 50% span (deg)	-75	-50
Rotor1 Inlet Metal Tip (deg)	-75	-55
Rotor1 Outlet Metal Hub (deg)	-60	-5
Rotor1 Outlet Metal 50% span (deg)	-65	-25
Rotor1 Outlet Metal Tip (deg)	-65	-35
Rotor2 Inlet Metal Hub (deg)	50	70
Rotor2 Inlet Metal 50% span (deg)	60	70
Rotor2 Inlet Metal Tip (deg)	60	70
Rotor2 Outlet Metal Hub (deg)	15	60
Rotor2 Outlet Metal 50% span (deg)	15	60
Rotor2 Outlet Metal Tip (deg)	30	60
Rotor i Interm. Metal Hub (*range)	0.2	0.8
Rotor i Interm. Metal Pos. Hub (*chord)	0.2	0.8
Rotor i Interm. Metal 50% span (*range)	0.2	0.8
Rotor i Interm. Metal Pos. 50% span (*c.)	0.2	0.8
Rotor i Interm. Metal Tip (*range)	0.2	0.8
Rotor i Interm. Metal Pos. Tip (*chord)	0.2	0.8
Rotor i Section1 Th. Pt1 (*chord)	0.001	0.004
Rotor i Section1 Th. Pt2 (*chord)	0.001	0.02
Rotor i Section1 Pos. Th. Pt2 (*chord)	0.2	0.8
Rotor i Section1 Th. Pt3 (*chord)	0.001	0.004
Rotor i Section2 Th. Pt1 (*chord)	0.001	0.002
Rotor i Section2 Th. Pt2 (*chord)	0.001	0.01
Rotor i Section2 Pos. Th. Pt2 (*chord)	0.2	0.8
Rotor i Section2 Th. Pt3 (*chord)	0.001	0.002
Rotor i Section3 Th. Pt1 (*chord)	0.001	0.002
Rotor i Section3 Th. Pt2 (*chord)	0.001	0.01
Rotor i Section3 Pos. Th. Pt2 (*chord)	0.2	0.8
Rotor i Section3 Th. Pt3 (*chord)	0.001	0.002
Rotor i Lean at Hub (*chord)	-0.1	0.1
Rotor i Lean at 50% span (*chord)	-0.1	0.1
Rotor i Lean at Tip (*chord)	-0.1	0.1
Rotor i Sweep at Hub (*chord)	-0.1	0.1
Rotor i Sweep at 50% span (*chord)	-0.1	0.1
Rotor i Sweep at Tip (*chord)	-0.1	0.1

Table 4.7: Design space for rotors design optimization

margin of at least 20% based on the yielding strength of Titanium. The objectives and constraints are:

- Maximize overall pressure ratio for high load
- Maximize adiabatic efficiency
- Constrain mass flow
- Constrain von Mises stress

An optimization of 50 generations with 40 individuals was performed. The whole process lasts for about two weeks using 40 processors, each evaluation (fluid and solid) taking about 6 hours of CPU time on a single processor. Surrogate models are usually used to accelerate such expensive optimization, but the high occurrence of non-converged flow solutions prevents to populate a database with a significant amount of individuals. To avoid the risk that the surrogate model predicts a minimum that could not be evaluated by the accurate solver, the authors decided not to use metamodels.

Figure 6 illustrates the optimization process with the progressive evolution towards populations that satisfy the structural constraint, i.e., maximal von Mises stress below 750MPa. After 50 generations a Pareto front appears and the optimal rotor configuration is selected as the individual offering the fore-most tradeoff of pressure ratio and efficiency (see large circle on Figure 4.21). The overall characteristics of the selected counterrotating compressor are summarized in Table 4.8.

4.3.3.3 Counterrotating compressor performance

To achieve high-pressure rise across the passages, both rotors operate with shock waves. Due to the high rotational speed of the wheels, the blade velocities exceed the

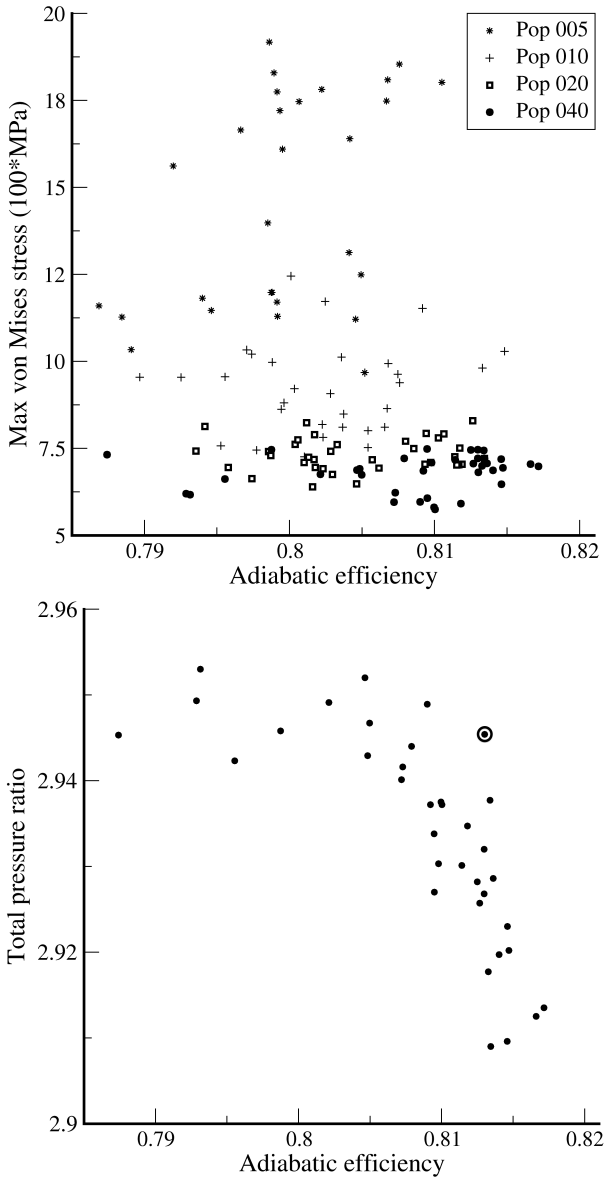

Figure 4.21: Evolution of populations for rotor optimization (top), Pareto front for rotor optimization (bottom)

Total pressure ratio	2.94
Adiabatic efficiency	0.813
Polytropic efficiency	0.838
Mass flow rate (kg/s)	20.42

Table 4.8: Optimum counterrotating compressor after 50 generations

local speed of sound, leading the surrounding flow to become supersonic. Figure 4.22 illustrates the inlet relative Mach number along the span for both rotors, compared to the sonic velocity (Mach 1 represented by a vertical dashed line).

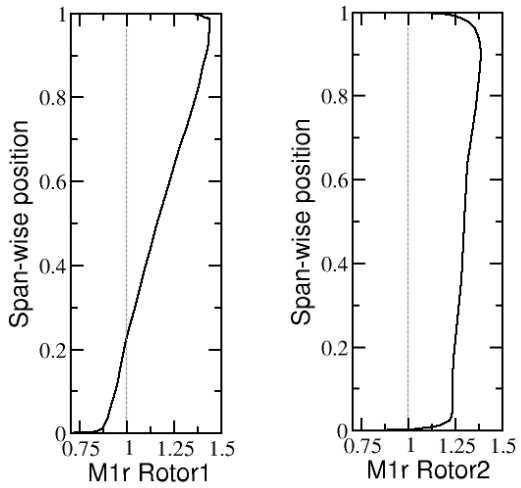

Figure 4.22: Span-wide distributions of inlet relative Mach number for finalized rotor 1 (left) and rotor 2 (right)

Figures 4.23 and 4.24 illustrate the blades with iso-density lines in the blade-to-blade plane, i.e. circumferential, at 15 and 85% of the span. Strong density gradients indicate the presence of shock waves. Series of periodic detached bow shocks can be observed at the leading edge of the rotors, except at the hub of the first rotor where the inlet relative Mach number remains subsonic (see Figure 4.22). Higher incoming Mach numbers lead to stronger shock waves and higher related losses. These structures are composed of a normal shock hitting the adjacent blade and an oblique shock that influences periodically the upstream flow. This behavior compares well with theoretical investigations that describe the unique incidence phenomena [65].

Figure 4.23: Density fields on circumferential plane at 15% span (first rotor on bottom and second rotor on top)

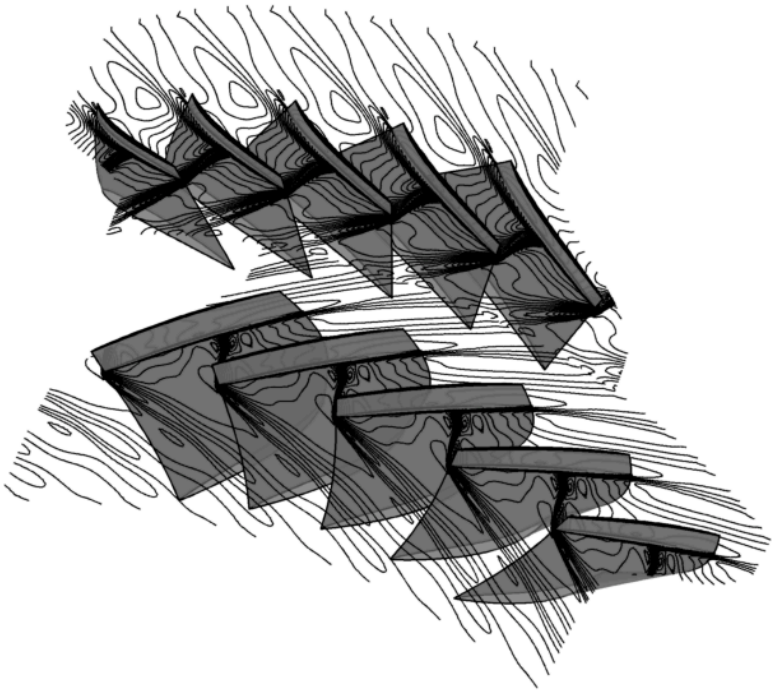

Figure 4.24: Density fields on circumferential plane at 85% span (first rotor on bottom and second rotor on top)

The preliminary design was performed considering empirical estimations of profile and shock losses. Figure 4.25 compares the entropy (i.e. loss) generation across the rotors between the flow path preliminary design and the finalized three-dimensional rotor geometries. After the extended optimization of the second cycle with three-dimensional high-fidelity solvers, the finalized performances are observed to remain in comparable ranges with the predictions of the low-fidelity one-dimensional model. Higher spans exhibit however larger losses, i.e. important entropy generation, for the finalized design. This can be explained by the tip clearance losses that the preliminary design did not consider. At the lower span, the entropy generated by the finalized rotors is clearly attenuated downstream of the second rotor compared to the predictions of the flow path model. A comparison of the span-wise distributions of relative flow angle obtained from the flow path preliminary design and the CFD based optimized geometry is presented in Figure 4.26. The finalized first rotor shows very good agreement with the prediction of the low-fidelity model. The second rotor exhibits a deficit of turning at the lower spans, which can be linked to the lower amount of loss observed in Figure 4.25.

The finalized rotors design satisfies the constraint of 20% safety margin to the yielding strength of titanium with a maximum von Mises stress of 684.14MPa and 302.25MPa in the first and second rotors respectively. Figure 4.27 highlights the shape of the hub fillet radius and displays the stress in the rotors. Peaks are observed on the first rotor; one just above the fillet, at about 20% of the chord from the leading edge; and a second at about 75% span and 75% of the chord where curvature of the blade appears to be high. In both cases, the features of the design methodology contributed to the successful design. The hub fillet prevents excessive stress at the junction between the blade and the root. In addition, the novel parameterization based on span-wise distributions provided a smooth curvature along the span, leading

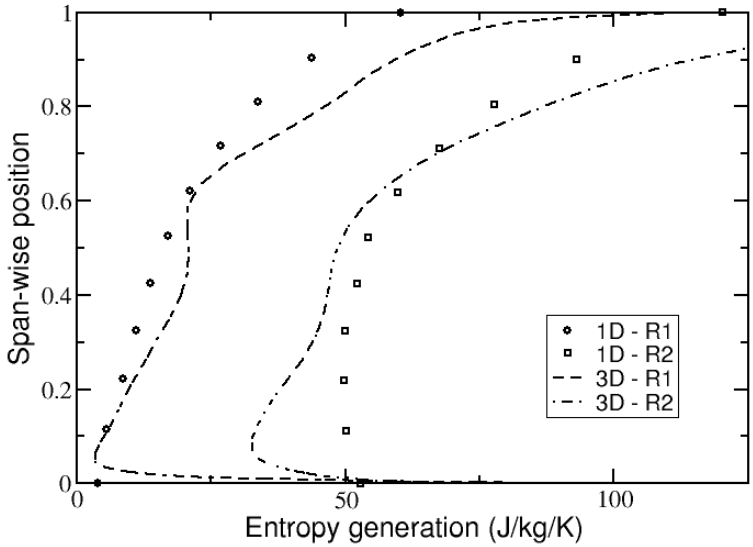

Figure 4.25: Span-wise distribution of entropy generation angles for preliminary and finalized designs

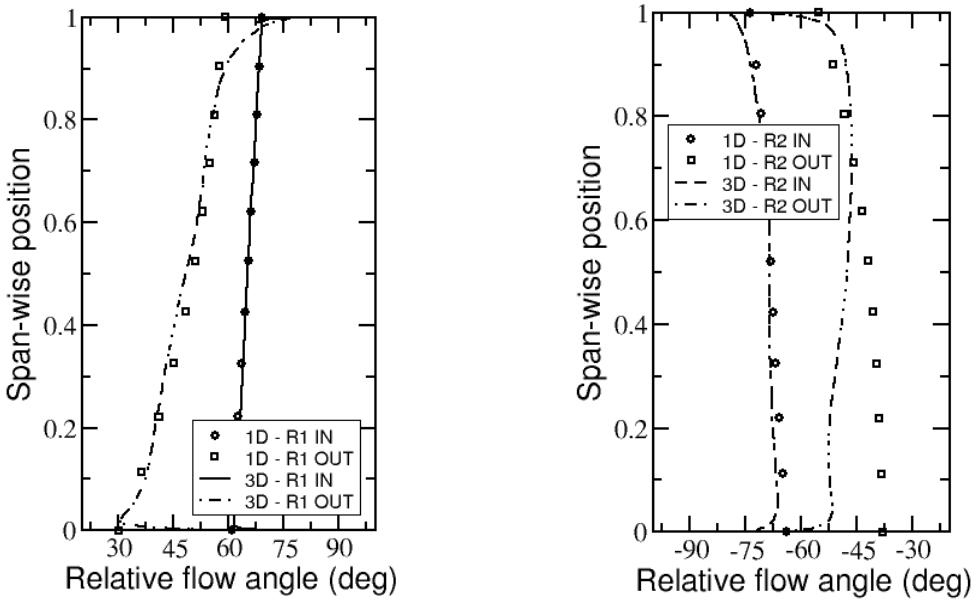

Figure 4.26: Span-wise distribution of relative flow angles for preliminary and finalized designs (rotor1 on left and rotor2 on right)

to a moderate and acceptable level of stress in the highly twisted blade.

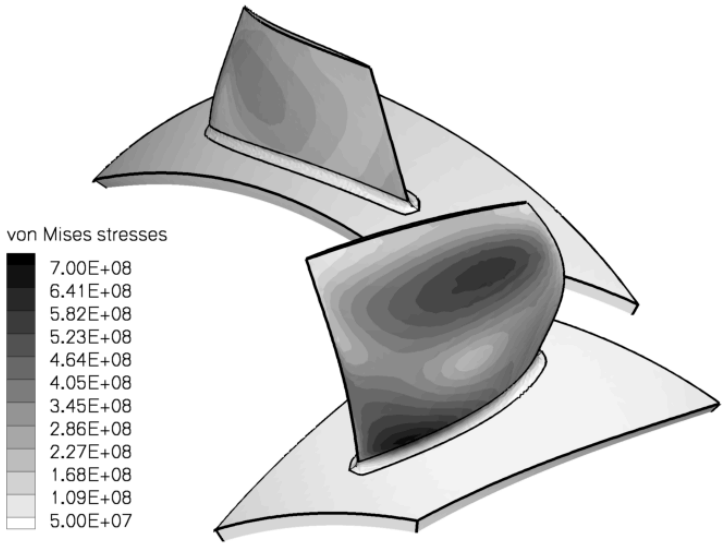

Figure 4.27: von Mises stress on both rotors

4.4 Conclusions

An integrated methodology to design a highly loaded and compact counterrotating compressor is presented. It is based on multifidelity, multidisciplinary evolutionary optimization, where Computational Fluid Dynamics (CFD) and Computational Structural Mechanics (CSM) performances are evaluated simultaneously.

The design of the flow path with a low-fidelity solver shows that optimization enables one to investigate a large set of candidates, while considering the three conflicting objectives of high load, low losses and compactness. The results are a set of non-dominated optima distributed along a Pareto front.

The three dimensional optimization is initialized based on the selected optimal flow path. A novel parameterization is developed to ease the handover between the

flow path definition and the geometry generation. It consists of span-wise distributions that provide smooth variations along the span; it also provides a convenient way to convert low-fidelity data into parameters of the detailed rotor geometry.

The final result shows that low-fidelity models can be employed for the design of supersonic compressors. Comparable level of entropy generation are observed between the CFD-based optimized geometry and the preliminary design predictions. The span-wise distributions of relative flow turning also appear similar with smooth evolutions along the span thanks to the parameterization. Both rotors encounter shock waves, whose behavior shows agreement with theoretical investigations of supersonic compressor profiles. Eventually, a high pressure ratio of 2.94 is achieved with an adiabatic efficiency of 81.3%.

From the structural point of view, both rotors provide a safety margin of 20% with regard to the yielding strength of titanium. The stress is distributed along the whole span with limited peaks. The maximal stress appears close to the hub, where the fillet is observed to limit the stress level. The novel parameterization contributed to limit the stress in high-twist regions, thanks to a smooth curvature along the span.

This proposed accelerated methodology requires a total computational time of 3 weeks on 40 processors. The novel parameterization developed with span-wise distributions enables one to reduce the time-to-market cost compared to conventional methodologies and to produce innovative configurations such as highly loaded and compact counterrotating compressors. It made the use of a strategy with only two successive optimizations possible, one with a through-flow and one with a three-dimensional multidisciplinary evaluation. This 1D-3D approach can be generalized to the design of other turbomachinery components.

5. SUMMARY

The scope of this dissertation is to investigate methodologies for aero-structural optimization of transonic turbines and compressors, with three main objectives:

- Evaluation of ν, k-ω, k-ϵ, and k-ϵ-v^2-f turbulence models
- Attenuation of unsteady shock interaction in high-pressure turbines
- Multi-fidelity, multi-disciplinary design optimization of counter-rotating fans

A RANS solver is implemented with different turbulence models: the one-equation model of Spalart-Allmaras, the two-equation SST k-ω model of Menter, the k-ϵ model with the Chien's damping functions, and the four-equation model k-ϵ-v^2-f. All show good agreement with experimental and theoretical data with the flow on a flat plate. A novel five-block topology is developed to control the grid refinement around the blade, in the throat passage, and in the wake area of a transonic turbine vane. The computation of the turbulent flow around this turbine vane case is possible for the Spalart-Allmaras model and the k-ϵ model, but encounters the occurrence of negative turbulence variables just downstream of the trailing edge with the k-ϵ-v^2-f model. Recommendations for alternative approaches to evaluate the four-equation turbulence model on turbomachinery applications are two-fold. A first option would be to compute the flow with an implicit solver, which may help with stability. A second option would be to consider more recent versions of the four equation model.

A soft computing methodology is proposed to reduce the unsteady forcing in high-pressure transonic turbines. It consists of an evolutionary optimization based on robust, high-fidelity flow simulations with low computational cost to attenuate the pressure distortion downstream of the vane. The optimization process is shown to be effective with 43.2% and 56.1% reductions of the pitch-wise static pressure dis-

tortion, for the 2D and 3D cases respectively. The optimal vane 2D section presents a convergent-divergent contraction channel, leading to an over-acceleration of the flow within the channel. The trailing edge shock system is modified and the resulting shock waves that propagate to the following blade row exhibit lower intensity. Subsequently to the vane optimization, the unsteady forcing on the rotor downstream of the optimal vane is computed with a non-linear harmonic method to evaluate the impact on the vane-rotor interaction. Attenuations up to 61% are observed and confirm the reduction in rotor high-cycle fatigue risk.

An integrated methodology to design a highly loaded and compact counterrotating compressor is presented. The design of the flow path with a low-fidelity solver shows that optimization enables one to investigate a large set of candidates. The three dimensional optimization is initialized based on the selected optimal flow path. A novel parameterization is developed to ease the handover between the flow path definition and the geometry generation. The final result shows that low-fidelity models can be employed for the design of supersonic compressors. Comparable level of entropy generation are observed between the CFD-based optimized geometry and the preliminary design predictions. Both rotors encounter shock waves, whose behavior shows agreement with theoretical investigations of supersonic compressor profiles. Eventually, a high pressure ratio of 2.94 is achieved with an adiabatic efficiency of 81.3%. From the structural point of view, both rotors provide a safety margin of 20% with regard to the yielding strength of titanium. The novel parameterization developed with span-wise distributions enables one to reduce the time-to-market cost compared to conventional methodologies and to produce innovative configurations such as highly loaded and compact counterrotating compressors. This 1D-3D approach can be generalized to the design of other turbomachinery components.

REFERENCES

[1] Heiser, W. H. and Pratt, D. T., *Hypersonic Airbreathing Propulsion*, AIAA Education Series, Washington D.C.: American Institute of Aeronautics and Astronautics, 1994.

[2] Rodriguez, M. I., Fernandez, V. V., and Paniagua, G., "Modeling, Analysis and Optimization of the Air Turbo Rocket Expander Engine", *Proceedings of 8th AIAA International Space Planes and Hypersonic Systems and Technologies Conference*, 2012.

[3] Wilcox, D. C., *Turbulence modeling for CFD*, Vol. 2, La Canada, CA: DCW Industries, 1998.

[4] Fonseca, C. and Fleming, P., "An overview of evolutionary algorithms in multiobjective optimization", *Evolutionary Computation*, Vol. 3, No. 1, 1995, pp. 1–16.

[5] Adeli, H. and Cheng, N.-T., "Integrated genetic algorithm for optimization of space structures", *Journal of Aerospace Engineering*, Vol. 6, No. 4, 1993, pp. 315–328.

[6] Sarma, K. C. and Adeli, H., "Fuzzy genetic algorithm for optimization of steel structures", *Journal of Structural Engineering*, Vol. 126, No. 5, 2000, pp. 596–604.

[7] Adeli, H. and Hung, S.-L., *Machine learning: neural networks, genetic algorithms, and fuzzy systems*, New York, NY: John Wiley & Sons, Inc., 1994.

[8] Adeli, H. and Kumar, S., "Concurrent structural optimization on massively parallel supercomputer", *Journal of Structural Engineering*, Vol. 121, No. 11, 1995, pp. 1588–1597.

[9] Beyer, H.-G. and Sendhoff, B., "Robust optimization–a comprehensive survey", *Computer Methods in Applied Mechanics and Engineering*, Vol. 196, No. 33, 2007, pp. 3190–3218.

[10] Chabuk, T., Reggia, J., Lohn, J., and Linden, D., "Causally-guided evolutionary optimization and its application to antenna array design", *Integrated Computer-Aided Engineering*, Vol. 19, No. 2, 2012, pp. 111–124.

[11] Spalart, P. and Allmaras, S., "A one-equation turbulence model for aerodynamic flows", *Proceedings of 30th Aerospace Sciences Meeting and Exhibit, AIAA Paper 92-0439*, 1992.

[12] Menter, F. R., "Two-equation eddy-viscosity turbulence models for engineering applications", *AIAA Journal*, Vol. 32, No. 8, 1994, pp. 1598–1605.

[13] Blazek, J., *Computational Fluid Dynamics: Principles and Applications: Principles and Applications*, Oxford, UK: Elsevier, 2001.

[14] Chien, K.-Y., "Predictions of channel and boundary-layer flows with a low-Reynolds-number turbulence model", *AIAA Journal*, Vol. 20, No. 1, 1982, pp. 33–38.

[15] Durbin, P., "Separated flow computations with the k-epsilon-v-squared model", *AIAA Journal*, Vol. 33, No. 4, 1995, pp. 659–664.

[16] Kalitzin, G., "Applications of the v2-f model to aerospace configurations", *Center for Turbulence Research, Annual Research Briefs*, 1999, pp. 289–300.

[17] Kline, S., Morkovin, M., and Sovran, G., "Computation of Turbulent Boundary Layers", *Proceedings of AFOSR-IFP-Stanford Conference*, 1968.

[18] Hanjalić, K., Popovac, M., and Hadžiabdić, M., "A robust near-wall elliptic-relaxation eddy-viscosity turbulence model for CFD", *International Journal of Heat and Fluid Flow*, Vol. 25, No. 6, 2004, pp. 1047–1051.

[19] Laurence, D., Uribe, J., and Utyuzhnikov, S., "A robust formulation of the v2-f

model", *Flow, Turbulence and Combustion*, Vol. 73, No. 3-4, 2005, pp. 169–185.

[20] Billard, F., Uribe, J. C., and Laurence, D., "A new formulation of the v2–f model using elliptic blending and its application to heat transfer prediction", *Proceedings of 7th Int. ERCOFTAC Symp. on Eng. Turb. Modelling and Measurements*, 2008.

[21] Jennions, I. and Adamczyk, J., "Evaluation of the interaction losses in a transonic turbine HP rotor/LP vane configuration", *ASME Journal of Turbomachinery*, Vol. 119, No. 1, 1997, pp. 68–76.

[22] Denton, J. and Xu, L., "The trailing edge loss of transonic turbine blades", *ASME Journal of Turbomachinery*, Vol. 112, No. 2, 1990, pp. 277–285.

[23] Giles, M., "Stator/rotor interaction in a transonic turbine", *Journal of Propulsion and Power*, Vol. 6, No. 5, 1990, pp. 621–627.

[24] Sieverding, C., Stanislas, M., and Snoeck, J., "The Base Pressure Problem in Transonic Turbine Cascades", *Journal of Engineering for Power*, Vol. 102, 1980, pp. 711–718.

[25] Ashworth, D., Grindrod, K., La Graff, J., and Schultz, D., "Unsteady aerodynamic and heat transfer processes in a transonic turbine stage", *Journal of Engineering for Gas Turbines Power*, Vol. 107, No. 4, 1985.

[26] Guennette, G., Epstein, A., Giles, M., Haimes, R., and Norton, R., "Fully Scaled Transonic Turbine Rotor Heat Transfer Measurement", *ASME Journal of Turbomachinery*, Vol. 111, 1989, pp. 1–7.

[27] Paniagua, G., Yasa, T., de la Loma, A., and Coton, T., "Unsteady strong shock interactions in a transonic turbine: experimental and numerical analysis", *Journal of Propulsion and Power*, Vol. 24, No. 4, 2008, pp. 722–731.

[28] Saracoglu, B., Paniagua, G., Salvadori, S., Tomasoni, F., Duni, S., Yasa, T., and Miranda, A., "Trailing edge shock modulation by pulsating coolant ejection",

Applied Thermal Engineering, Vol. 48, 2012, pp. 1–10.

[29] Madavan, N., Rai, M., and Huber, F., "Neural net-based redesign of transonic turbines for improved unsteady aerodynamic performance", *NASA Technical Memorandum*, , No. 8889, 1998.

[30] Rai, M., Madavan, N., and Huber, F., "Improving the Insteady Aerodynamic Performance of Transonic Turbines Using Neural Networks", *NASA Technical Memorandum*, , No. 208791, 1999.

[31] Shelton, M. and Gregory, B., "Optimization of a Transonic Turbine Airfoil using Artificial Intelligence, CFD and Cascade Testing", *Proceedings of International Gas Turbine and Aeroengine Congress and Exposition*, 1993.

[32] Vilmin, S., Lorrain, E., Hirsch, C., and Swoboda, M., "Unsteady flow modeling across the rotor/stator interface using the nonlinear harmonic method", *Proceedings of ASME Turbo Expo 2002: Power for Land, Sea, and Air*, , No. 90210, 2006.

[33] Storn, R. and Price, K., "Differential evolution–a simple and efficient heuristic for global optimization over continuous spaces", *Journal of Global Optimization*, Vol. 11, No. 4, 1997, pp. 341–359.

[34] Das, S. and Suganthan, P. N., "Differential evolution: A survey of the state-of-the-art", *Evolutionary Computation*, Vol. 15(1), 2011, pp. 4–31.

[35] Madavan, N., "Multiobjective optimization using a Pareto differential evolution approach", *Proceedings of the 2002 Congress on Evolutionary Computation*, Vol. 2, 2002, pp. 1145–1150.

[36] Deb, K., Pratap, A., Agarwal, S., and Meyarivan, T., "A fast and elitist multiobjective genetic algorithm: NSGA-II", *Evolutionary Computation, IEEE Transactions*, Vol. 6, No. 2, 2002, pp. 182–197.

[37] Arnone, A., "Viscous analysis of three-dimensional rotor flow using a multigrid

method", *ASME Journal of Turbomachinery*, Vol. 116, No. 3, 1994, pp. 435–445.

[38] Bradshaw, P., "Turbulence modeling with application to turbomachinery", *Progress in Aerospace Sciences*, Vol. 32, No. 6, 1996, pp. 575 – 624.

[39] Sieverding, C., Arts, T., Denos, R., and Martelli, F., "Investigation of the flow field downstream of a turbine trailing edge cooled nozzle guide vane", *ASME Journal of Turbomachinery*, Vol. 118, No. 2, 1996, pp. 291–300.

[40] He, L., Chen, T., Wells, R., Li, Y., and Ning, W., "Analysis of rotor-rotor and stator-stator interferences in multi-stage turbomachines", *ASME Journal of Turbomachinery*, Vol. 124, No. 4, 2002, pp. 564–571.

[41] Nouri, H., Ravelet, F., Bakir, F., and Sarraf, C., "Design and Experimental Validation of a Ducted Counter-rotating Axial-flow Fans System", *Journal of Fluids Engineering*, Vol. 134, 2012.

[42] Schimming, P., "Counter Rotating Fans - An Aircraft Propulsion for the Future?" *Journal of Thermal Sciences*, Vol. 12, No. 2, 2003.

[43] Wilcox, W. W., "An Analysis of the Potentialities of a Two-Stage Counterrotation Supersonic Compressor", Research Memorandum E52E01, NACA, 1952.

[44] Wilcox, W. W. and Wright, L. C., "Investigation of Two-Stage Counterrotating Compressor III - Design of Second-Stage Rotor and Preliminary Over-All Performance", Research Memorandum E56G30a, NACA, 1956.

[45] Minato, R., Kato, D., Higashino, K., and Tanatsugu, N., "Development Study on Counter Rotating Fan Jet Engine for Supersonic Flight", *Proceedings of International Society for Air Breathing Engines*, , No. 1233, 2011.

[46] Parker, D. V., *Design and operation of a counter-rotating aspirated compressor blowdown test facility*, Ph.D. thesis, Massachusetts Institute of Technology, 2005.

[47] Lian, Y. and Liou, M., "Aerostructural Optimization of a Transonic Compressor

Rotor", *Journal of Propulsion and Power*, Vol. 22, No. 4, 2006, pp. 880–888.

[48] Mueller, L., Alsalihi, Z., and Verstraete, T., "Multidisciplinary Optimization of a Turbocharger Radial Turbine", *ASME Journal of Turbomachinery*, Vol. 135, No. 2, 2013.

[49] Okui, H., Verstraete, T., Van den Braembussche, R., and Alsalihi, Z., "Three-Dimensional Design and Optimization of a Transonic Rotor in Axial Flow Compressors", *ASME Journal of Turbomachinery*, Vol. 135, No. 3, 2013.

[50] Verstraete, T., Alsalihi, Z., and den Braembussche, R. A. V., "Multidisciplinary Optimization of a Radial Compressor for Microgas Turbine Applications", *ASME Journal of Turbomachinery*, Vol. 132, No. 3, 2010.

[51] Calvert, W. and Ginder, R., "Transonic fan and compressor design", *Proceedings of the Institution of Mechanical Engineers, Part C: Journal of Mechanical Engineering Science*, Vol. 213, No. 5, 1999, pp. 419–436.

[52] Cunnan, W. S., Urasek, D. C., and Stevans, W., *Design and performance of a 427-meter-per-second-tip-speed two-stage fan having a 2.40 pressure ratio*, Washington D.C.: National Aeronautics and Space Administration, Scientific and Technical Information Office, 1978.

[53] Sanger, N., "Design of a low aspect ratio transonic compressor stage using CFD techniques", *ASME Journal of Turbomachinery*, Vol. 118, No. 3, 1996.

[54] Reid, L. and Moore, R., *Design and overall performance of four highly loaded, high speed inlet stages for an advanced high-pressure-ratio core compressor*, Washington D.C.: National Aeronautics and Space Administration, Scientific and Technical Information Office, 1978.

[55] Merchant, A., *Design and analysis of axial aspirated compressor stages*, Ph.D. thesis, Massachusetts Institute of Technology, 9 1999.

[56] Dickens, T. and Day, I., "The Design of Highly Loaded Axial Compressors",

ASME Journal of Turbomachinery, Vol. 133, No. 3, 2011.

[57] Lieblein, S., Schwenk, F., and Broderick, R., *Diffusion Factor for Estimating Losses and Limiting Blade Loadings in Axial Flow Compressor Blade Elements*, Washington D.C.: National Aeronautics and Space Administration, Scientific and Technical Information Office, 1953.

[58] Miller, G., Lewus, G., and Hartmann, M., "Shock Losses in Transonic Rotor Rows", *Journal of Engineering for Power*, Vol. 83, 1961, pp. 235–242.

[59] Lakshminarayana, B., *Fluid Dynamics and Heat Transfer of Turbomachinery*, New York, NY: John Wiley & Sons, Inc, 1996.

[60] Dhondt, G., *The finite element method for three-dimensional thermomechanical applications*, West Sussex, England: John Wiley & Sons, Inc, 2004.

[61] Shepard, D., "A two-dimensional interpolation function for irregularly-spaced data", *Proceedings of the 1968 23rd ACM national conference*, 1968, pp. 517–524.

[62] Lian, Y. and Liou, M.-S., "Aerostructural optimization of a transonic compressor rotor", *Journal of Propulsion and Power*, Vol. 22, No. 4, 2006, pp. 880–888.

[63] Lichtfuss, H. and Starken, H., "Supersonic cascade flow", *Progress in Aerospace Sciences*, Vol. 15, 1974, pp. 37–149.

[64] Joly, M. M., Verstraete, T., and Paniagua, G., "Multidisciplinary design optimization of a compact highly loaded fan", *Structural and Multidisciplinary Optimization*, Vol. 49, No. 3, 2013, pp. 471–483.

[65] Lichtfuss, H. J. and Starken, H., "Supersonic Cascade Flow", *Progress in Aerospace Sciences*, Vol. 15, 1974, pp. 37–149.

[66] Denton, J. D., "Loss Mechanisms in Turbomachines", *ASME Journal of Turbomachinery*, Vol. 115, 1993, pp. 621–656.